JCB Journal of Cell Biology

ARTICLE

PI(4,5)P2 determines the threshold of mechanical force–induced B cell activation

Zhengpeng Wan[1], Chenguang Xu[1*], Xiangjun Chen[1*], Hengyi Xie[1*], Zongyu Li[1*], Jing Wang[1*], Xingyu Ji[1], Haodong Chen[2], Qinghua Ji[3], Samina Shaheen[1], Yang Xu[4], Fei Wang[2], Zhuo Tang[2], Ji-Shen Zheng[4], Wei Chen[5], Jizhong Lou[3], and Wanli Liu[1,6]

B lymphocytes use B cell receptors (BCRs) to sense the chemical and physical features of antigens. The activation of isotype-switched IgG-BCR by mechanical force exhibits a distinct sensitivity and threshold in comparison with IgM-BCR. However, molecular mechanisms governing these differences remain to be identified. In this study, we report that the low threshold of IgG-BCR activation by mechanical force is highly dependent on tethering of the cytoplasmic tail of the IgG-BCR heavy chain (IgG-tail) to the plasma membrane. Mechanistically, we show that the positively charged residues in the IgG-tail play a crucial role by highly enriching phosphatidylinositol (4,5)-biphosphate (PI(4,5)P2) into the membrane microdomains of IgG-BCRs. Indeed, manipulating the amounts of PI(4,5)P2 within IgG-BCR membrane microdomains significantly altered the threshold and sensitivity of IgG-BCR activation. Our results reveal a lipid-dependent mechanism for determining the threshold of IgG-BCR activation by mechanical force.

Introduction

B lymphocytes are responsible for the antibody responses arising from the recognition of pathological antigens by the surface-expressed B cell receptor (BCR; Pierce and Liu, 2010; Xu et al., 2014; Liu et al., 2016a). The BCR is composed of a membrane-bound immunoglobulin (mIg) and a noncovalently associated heterodimer of Igα and Igβ in a 1:1 mIg/Igα-Igβ heterodimer stoichiometry (Schamel and Reth, 2000; Tolar et al., 2005). BCR is an extraordinary receptor that can efficiently discriminate among a wide variety of chemical and physical features of antigens (Liu et al., 2016a) including antigen density (Fleire et al., 2006; Liu et al., 2010a; Tang et al., 2016; Wang et al., 2016), affinity (Fleire et al., 2006; Liu et al., 2010a), valency (Bachmann et al., 1993; Liu et al., 2004; Liu and Chen, 2005), Brownian mobility feature of antigen (Wan and Liu, 2012), the mechanical forces delivered to the BCRs by the antigens (Natkanski et al., 2013; Wan et al., 2015), and the stiffness feature of antigen-presenting substrates (Wan et al., 2013; Zeng et al., 2015; Shaheen et al., 2017). This discriminatory capacity plays a key role in B cell activation. Thus, elucidating the molecular mechanisms that enable B cells to discriminate among different antigens will provide important insights into how they develop the high-affinity antibodies crucial for an effective immune response.

Moreover, B cells exploit different BCR isotypes to recognize antigens and initiate transmembrane-activating signaling. Mature naive B cells use IgM- and IgD-BCRs, whereas memory B cells, which are responsible for the rapid antigen recall humoral responses upon vaccine immunization, mainly use isotype-switched IgG-BCRs (McHeyzer-Williams and McHeyzer-Williams, 2005; Pierce and Liu, 2010). Physical cues from the antigen can regulate B cell activation by applying a mechanical force on the BCR and have diverse effects on the different B cell subsets (Tolar, 2017). For example, compared with naive B cells, germinal center B cells apply more persistent and stronger tensile forces on the BCR. This negatively regulates antigen binding by using myosin II contractility to achieve more strict affinity discrimination during antigen extractions from immunological synapses (Nowosad et al., 2016). By using a double-stranded DNA (dsDNA)-based tension gauge tether (TGT) as a mechanical force sensor, we recently showed that IgM-BCR activation is highly dependent on mechanical forces, with the level of activation dependent on the amount of force (Wan et al., 2015). In contrast, the activation of isotype-switched IgG-BCR only requires a lower threshold of <12 pN (Wan et al., 2015). However, molecular mechanisms regulating these distinct thresholds of IgM-BCR

[1]Ministry of Education Key Laboratory of Protein Sciences, Collaborative Innovation Center for Diagnosis and Treatment of Infectious Diseases, School of Life Sciences, Institute for Immunology, Tsinghua University, Beijing, China; [2]Natural Products Research Center, Chengdu Institution of Biology, Chinese Academy of Science, Chengdu, China; [3]Laboratory of RNA Biology, Institute of Biophysics, Chinese Academy of Sciences, Beijing, China; [4]School of Life Sciences, University of Science and Technology of China, Hefei, China; [5]School of Basic Medical Sciences, Zhejiang University, Hangzhou, China; [6]Beijing Key Laboratory for Immunological Research on Chronic Diseases, Beijing, China.

*C. Xu, X. Chen, H. Xie, Z. Li, and J. Wang contributed equally to this paper; Correspondence to Wanli Liu: liuwanli@biomed.tsinghua.edu.cn.

versus IgG-BCR remain to be identified. In this study, we discover that the evolutionarily conserved cytoplasmic tail of the IgG-BCR heavy chain (IgG-tail) is responsible for the localized phosphatidylinositol (PI) (4,5)-biphosphate (PI(4,5)P2) enrichment by its PM-tethered and positively charged residues at resting stage, resulting in the low threshold of IgG-BCR activation by mechanical force.

Results

Activation of IgA-, IgD-, and IgM-BCR exhibit distinct mechanical force thresholds compared with IgE- or IgG-BCR

To investigate the mechanical force–induced activation of different isotypes of BCRs, we constructed 4-hydroxy-3-nitrophenylacetyl (NP)-specific TGTs (NP-TGTs) to stimulate B1-8–specific BCRs with different amounts of mechanical force as described previously (Wan et al., 2015). In brief, each NP-TGT molecule is composed of two single-stranded DNA (ssDNA) molecules with specific modifications (Fig. 1 A). The first ssDNA molecule is biotin conjugated at three distinct positions to provide a defined range of rupture force (12, 43, and 56 pN), whereas the second ssDNA molecule is conjugated at the 3′ terminus with the B1-8 BCR–specific antigen NP. The activation of the BCRs is evaluated by quantifying the synaptic accumulation of both BCRs and phosphorylated spleen tyrosine kinase (Syk) in response to these NP-TGT mechanical force sensors (12, 43, and 56 pN) using total internal reflection fluorescence microscopy (TIRFM) imaging (Wan et al., 2015).

There are five isotypes of membrane-bound BCR: IgM-, IgD-, IgA-, IgG-, and IgE-BCR, which have distinctive constant regions and heavy chain cytoplasmic tails. We tested mechanical force–induced activation of all five isotypes of membrane-bound BCRs by constructing NP-specific human BCRs comprising the constant region of IgM-, IgD-, IgA-, IgG- and IgE-BCR combined with the B1-8 NP–specific variable region. IgM-, IgD-, and IgA-BCR shared the same multithreshold activation features: accumulation of BCRs was the strongest on high–mechanical force (56 pN) NP-TGTs, relatively moderate on medium–mechanical force NP-TGTs, and weak on low–mechanical force (12 pN) NP-TGTs. This indicates multiple mechanical force thresholds for the activation of IgM-, IgD-, and IgA-BCRs (Fig. 1, B–D). In marked contrast, IgG- and IgE-BCRs possess low-threshold characteristics as the recruitment of these BCRs was equally good on each of the 12-pN, 43-pN, and 56-pN NP-TGT surfaces (Fig. 1, E and F), consistent with our previous study (Wan et al., 2015). Further tests on downstream signaling of IgM- and IgG-BCR showed that the activation of MAPK (ERK) is positively correlated with the degree of BCR accumulation on the NP-TGT surfaces (Fig. 1, G–I).

The low–mechanical force threshold of IgG-BCR activation is not dependent on the immunoglobulin tail tyrosine (ITT) or PDZ-binding motif within the IgG-tail

Our previous study and the data in this study established a critical role for the conserved IgG-tail in lowering the threshold of mechanical force to induce IgG-BCR activation (Wan et al., 2015). There are two important motifs within the IgG-tail: the ITT motif and the PDZ-binding motif. When phosphorylated, the ITT motif (YKNM in IgG-tail) provides the binding site for growth factor receptor-bound protein 2 (GRB2), which together recruit BTK to enhance signaling transduction (Engels et al., 2009). The PDZ-binding motif (SSVV in the IgG-tail) provides the capacity to interact with SAP97, a PDZ motif–containing scaffold protein of the synapse-associated protein family, enhancing the formation of IgG-BCR microclusters (Liu et al., 2012). To investigate the contribution of these two motifs in lowering the threshold of mechanical force required to induce IgG-BCR activation, we constructed two mutant IgG-BCRs, YKNM to FKNM (Y/F) and SSVV/AAAA, to impair the function of the ITT motif and PDZ-binding motif, respectively (Fig. 1 J). These two mutant IgG-BCRs exhibited the same low threshold pattern as WT IgG-BCRs in response to NP-TGTs (Fig. 1, K and L). Thus, the low–mechanical force threshold of IgG-BCR activation is not dependent on the ITT or PDZ-binding motif within the IgG-tail.

The plasma membrane (PM)-tethered status of the IgG-tail is required for the low–mechanical force threshold during its activation

Our previous study revealed that the IgG-tail in memory B cells interacted with the inner leaflet of the membrane at resting stage (Chen et al., 2015). Therefore, we investigated whether the PM-tethered status of the IgG-tail affects the threshold of mechanical force required to induce IgG-BCR activation. We rationally designed and constructed a series of IgG-BCR mutants with different PM-tethering status by modifying the sequence of the IgG-tail (Fig. S5). These mutants largely expressed similar BCRs on the PM as WT IgG-BCR (Fig. S1). We further examined their membrane-anchoring status in quiescent B cells by a fluorescence resonance energy transfer (FRET) assay following our published protocol (Chen et al., 2015). In brief, we fused the FRET donor, monomeric teal fluorescent protein (TFP; mTFP) to the C terminus of the membrane-bound IgG-tail (WT or mutant) and used the fluorescent membrane dye octadecyl rhodamine B (R18) as a FRET acceptor to stain the PM. As a positive control, the WT IgG-tail strongly associated with the inner leaflet of the PM as indicated by the high FRET efficiency between the IgG-tail–fused mTFP and R18 (Fig. 2 A), consistent with our previous research (Chen et al., 2015).

First, we detached the IgG-tail from the inner leaflet of the PM by inserting a flexible 25-aa linker between the transmembrane domain of mIgG and the N terminus of the IgG-tail (Fig. 2, A and B; Chen et al., 2015). We validated that both the 25 aa alone (Mut1) as a flexible linker control and the 25 aa–inserted IgG-tail (Mut2) dissociated from the PM by showing significantly lower FRET efficiency in comparison with the WT IgG-BCR (Fig. 2, C and D). When we analyzed the mechanical force–induced activation, we found that Mut1 and Mut2 now reacted to NP-TGTs in a multithreshold manner similar to that of WT IgM-BCR. This suggests that PM association of the cytoplasmic tail of IgG-BCR is required for the low–mechanical force threshold of activation (Fig. 2, E and F; see also Fig. 9).

The association of the IgG-tail with the inner leaflet of the PM is dependent on its positively charged and hydrophobic amino acid residues. The positively charged residues can interact with negatively charged acidic phospholipids, and the hydrophobic residues can be buried in the hydrophobic core of the membrane

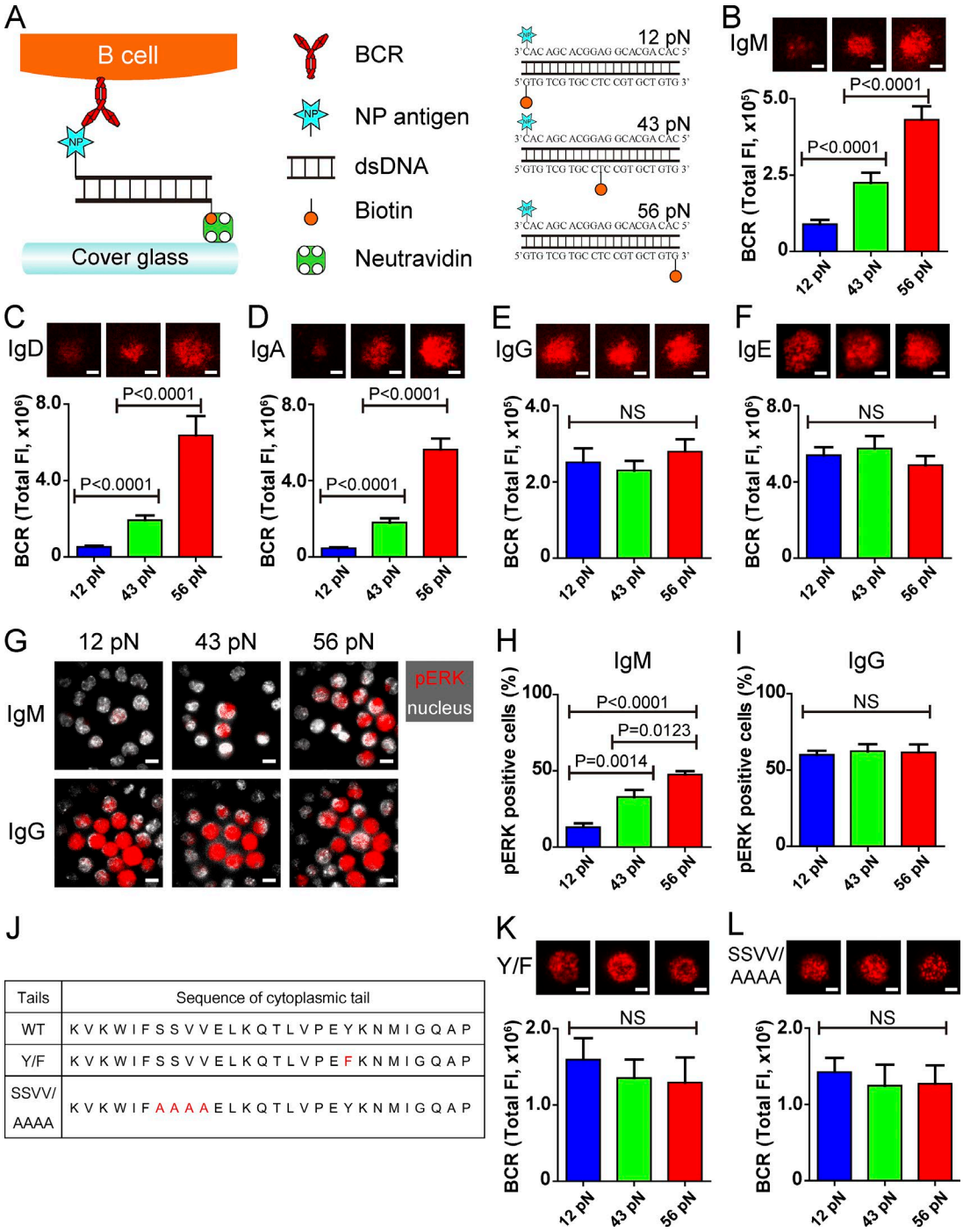

Figure 1. **Activation of IgA-, IgD-, and IgM-BCR exhibit distinct mechanical force thresholds compared with IgE- or IgG-BCR. (A)** Schematic representation of the NP-specific BCR-expressing B cells and NP-TGTs with the predefined tension forces of 12 pN, 43 pN, and 56 pN, respectively, which are mainly used in this study. **(B–F)** Representative TIRFM images and quantification of the total FI of BCR accumulation into immunological synapse in contact with 12-pN, 43-pN, and 56-pN NP-TGTs in Ramos B cells expressing NP-specific IgM-BCR (B), IgD-BCR (C), IgA-BCR (D), IgG-BCR (E), and IgE-BCR (F), respectively. **(G–I)** Representative fluorescent images (G) and quantifications of the percentage of pERK-positive J558L cells expressing IgM-BCR (H) or IgG-BCR (I) in response to NP-TGTs. Cells were stained with an antibody to phosphorylated ERK (red) and a nucleus dye Hoechst (white). About 70–110 cells were scored for each data point. **(J)** Sequence of WT, Y/F, and SSVV/AAAA cytoplasmic tails. **(K and L)** Representative TIRFM images and quantification of the total FI of BCR recruitment into immunological synapses on contact surfaces of 12-pN, 43-pN, and 56-pN NP-TGTs in J558L cells expressing NP-specific IgG-BCR with cytoplasmic mutations of Y/F to block the ITT signaling motif (K) or SSVV/AAAA to block the PDZ-binding motif (L). Error bars represent means ± SEM. Two-tailed *t* tests were performed for the statistical comparisons. Data are from at least 25 cells and represent at least two independent experiments. Bars: (B–F, K, and L) 3 µm; (G) 9 µm.

lipids. Considering these two criteria, we constructed another four mutant IgG-BCRs by mutating the positively charged and/or hydrophobic residues (Fig. 3 A). Both Mut3 and Mut4 were designed to decrease the proportion of positively charged amino acids as shown by the decreased isoelectric point (pI) and the reduced hydrophobic level of the IgG-tail of these two mutants

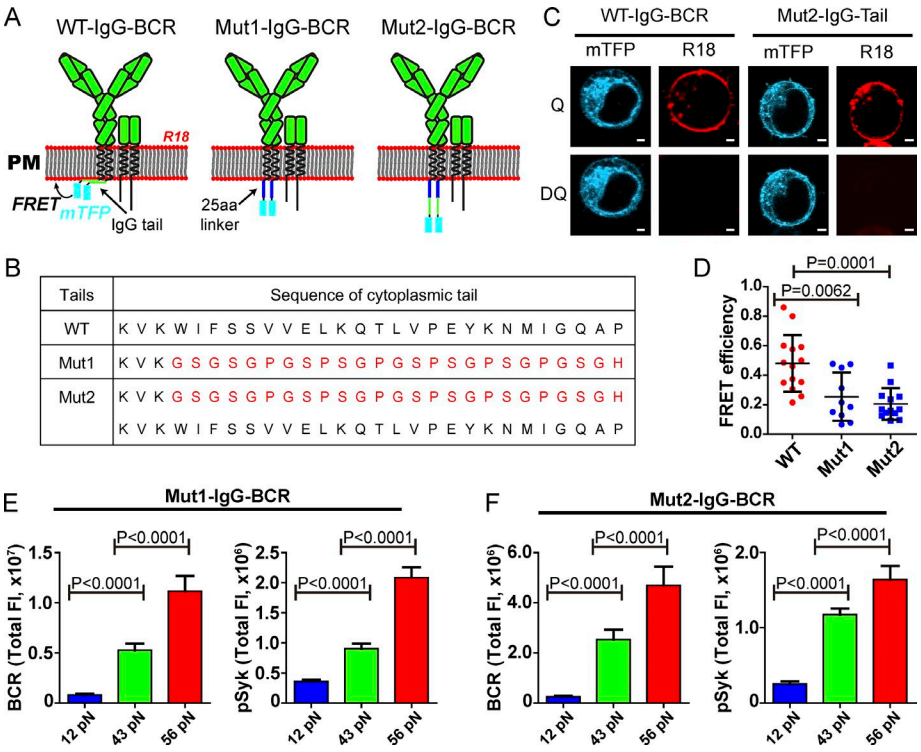

Figure 2. **The PM-tethered status of the IgG-tail is required for the low threshold of mechanical force–induced activation. (A)** Schematic illustration showing the FRET system that was used to detect the interaction between mTFP (FRET donor) fused to the C terminus of the cytoplasmic tail (WT, Mut1, and Mut2) and R18 dye (FRET acceptor) stained on the PM. **(B)** Sequence of the cytoplasmic tail of WT, Mut1 (the flexible 25 aa), and Mut2 (inserting a 25-aa flexible linker between the transmembrane domain of the IgG-BCR and N terminus of the IgG-tail). **(C and D)** Dequenching FRET to measure the FRET efficiency between mTFP and R18 in WT, Mut1–, and Mut2–IgG-BCR–expressing DT40 B cells. FRET efficiency was calculated as detailed in Materials and methods. DQ, dequenched; Q, quenched. **(C)** Representative confocal images of DT40 B cells expressing WT and Mut2–IgG-BCR are shown. Bars, 1.1 µm. **(D)** FRET efficiency was measured and plotted. Error bars represent means ± SD. **(E and F)** Statistical quantification of the synaptic recruitment of IgG-BCR and pSyk in J558L cells expressing Mut1– (E) or Mut2–IgG-BCR (F). Error bars represent means ± SEM. Two-tailed *t* tests were performed for the statistical comparisons. Data are from at least 30 cells over three independent experiments.

in comparison with that of the WT IgG-tail. Mut5 was designed to keep the hydrophobic level intact but reduce the pI value of its cytoplasmic tail, whereas Mut6 was designed to keep the pI value intact but decrease the hydrophobicity compared with that of the WT IgG-tail (Fig. 3 A). All the cytoplasmic tails of these four mutant IgG-BCRs were dissociated from the PM as demonstrated by the drastically decreased FRET efficiencies between the IgG-tail–fused mTFP and R18 (Fig. 3, B–D). Thus, both the hydrophobic and positively charged residues on the IgG-tails are important for its PM association. Consistent with results for Mut1 and Mut2, when reacting to NP-TGTs, Mut3, Mut4, Mut5, and Mut6 also showed a typical multithreshold pattern similar to that of WT IgM-BCR, indicating the loss of the low-mechanical force threshold feature (Fig. 3, E–H; see also Fig. 9). Additionally, we found that the motilities of WT, Mut5–, and Mut6–IgG-BCRs were different in response to NP-TGTs. WT IgG-BCR moved faster at resting stage than Mut5–IgG-BCR and Mut6–IgG-BCR and significantly slowed down when encountering either 56-pN or 12-pN NP-TGTs. In contrast, Mut5– and Mut6–IgG-BCR only slowed down when encountering 56-pN NP-TGTs but not 12-pN NP-TGTs (Fig. 4). These results showed that the low-mechanical force threshold of IgG-BCR is dependent on the PM-tethered status of IgG-tail, the topology of which is mediated by both its hydrophobic and positively charged residues.

Positively charged residues in the PM-tethered IgG-tail are responsible for the low-mechanical force threshold of IgG-BCR activation

Furthermore, we designed several IgG-BCR with mutant IgG-tails by increasing positively charged residues (Mut7), reducing the hydrophobic and increasing the negatively charged residues (Mut8 as control for Mut7), or enhancing the hydrophobic level and keeping it almost electroneutral (Mut9 and Mut10). Mut7, Mut9, and Mut10 were theoretically and experimentally tethered to the PM in quiescent B cells as quantified by the abovementioned FRET assay (Fig. 5, A–D). Unexpectedly, only the positively charged mutant tail (Mut7) but not the other mutants (Mut9 and Mut10) displayed the low-mechanical force threshold pattern similar to WT IgG-BCR activation (Fig. 5, E–H; see also Fig. 9). Furthermore, IgM-BCRs equipped with the positively charged cytoplasmic tail of Mut7 were also able to lower the mechanical force threshold for IgM-BCR activation (Fig. S2, A–C). Thus, the presence of the positively charged residues of PM-tethered IgG-tail is mainly responsible for lowering the threshold on IgG-BCR activation by mechanical force.

The WT IgG-tail enriches PI(4,5)P2 on the PM in quiescent B cells

Our previous research demonstrated that the positively charged residues of the IgG-tail interact with acidic phospholipids in the inner leaflet of the PM (Chen et al., 2015). The IgG-tail may recruit acidic phospholipids, which are known to be involved in signaling transduction in many types of cells (Falkenburger et al., 2010), through its positively charged residues. Therefore, we speculated that acidic phospholipids may be responsible for IgG-BCR activation by lowering the threshold of mechanical forces. To validate our hypothesis, we screened the enrichment of different types of acidic phospholipids, including phosphatidylserine (PS), PI(4,5)P2, PI (3,4,5)-trisphosphate (PI(3,4,5)P3), and phosphatidic acid (PA), into the WT IgG-BCR membrane microdomains on the PM by superresolution imaging of mEos3.2-based lipid-specific biosensors. We used the PH domain

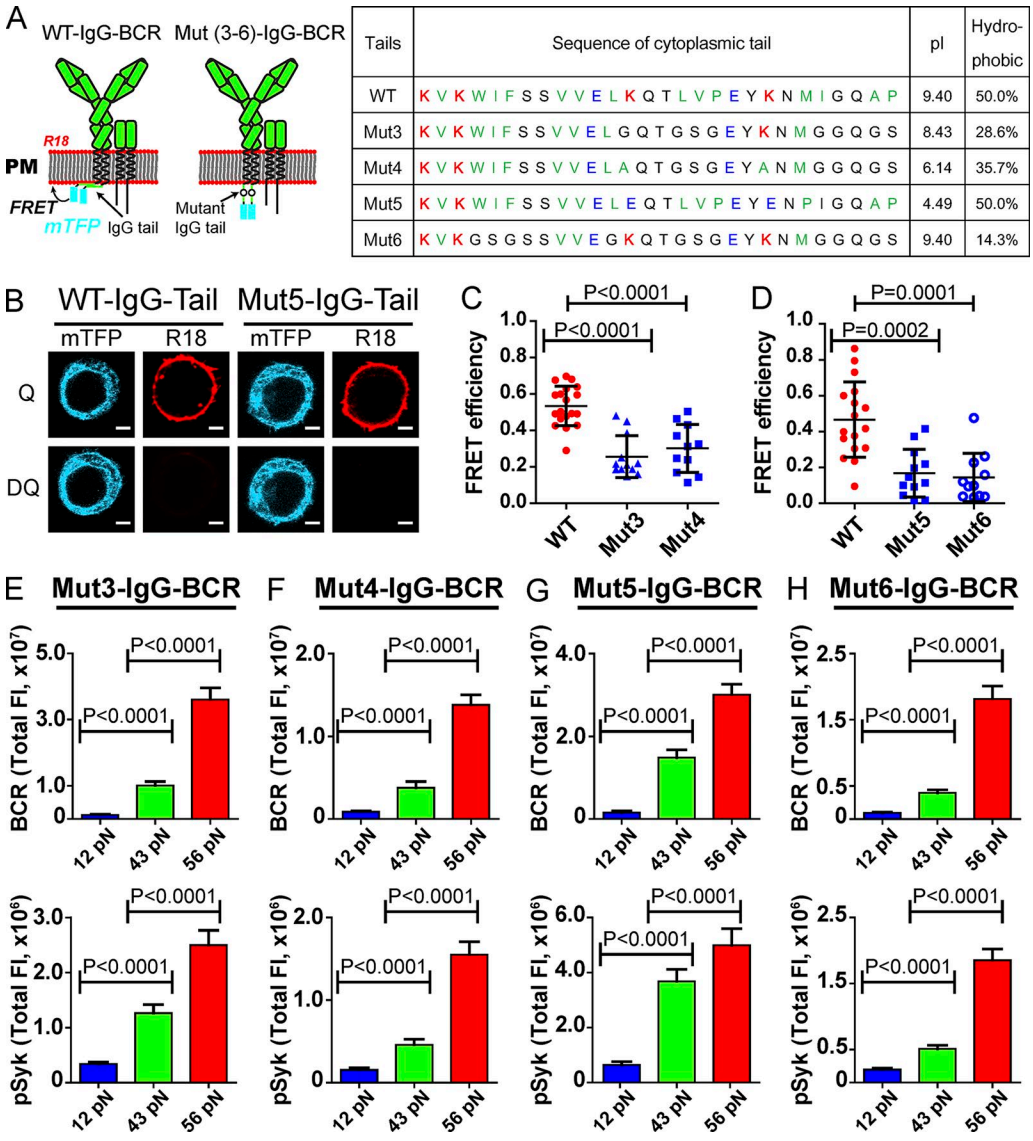

Tails	Sequence of cytoplasmic tail	pI	Hydrophobic
WT	K V K W I F S S V V E L K Q T L V P E Y K N M I G Q A P	9.40	50.0%
Mut3	K V K W I F S S V V E L G Q T G S G E Y K N M G G Q G S	8.43	28.6%
Mut4	K V K W I F S S V V E L A Q T G S G E Y A N M G G Q G S	6.14	35.7%
Mut5	K V K W I F S S V V E L E Q T L V P E Y E N P I G Q A P	4.49	50.0%
Mut6	K V K G S G S S V V E G K Q T G S G E Y K N M G G Q G S	9.40	14.3%

Figure 3. **Both positively charged and hydrophobic features of IgG-tail are important for its PM association orientation. (A)** Left: Schematic illustration showing the FRET system to detect the interaction between mTFP (FRET donor) fused to the C terminus of the cytoplasmic tail (WT or Mut (3–6)) and R18 dye (FRET acceptor) stained on the PM. Right: Sequence and biochemical characteristic analysis of the cytoplasmic tail of WT, Mut3/4 (reducing both hydrophobicity and positively charged proportion of IgG-tail), Mut5 (keeping hydrophobic level intact but reducing the pI value), and Mut6 (keeping pI value intact but decreasing hydrophobicity). Acidic, basic, and hydrophobic residues are colored in blue, red, and green, respectively. **(B–D)** Dequenching FRET to measure the FRET efficiency between mTFP and R18 in WT, Mut3–, Mut4–, Mut5–, and Mut6–IgG-BCR–expressing DT40 B cells. **(B)** FRET efficiency was calculated as detailed in Materials and methods. Representative confocal images of WT and Mut5-IgG-BCR are shown. Bars, 1.1 µm. DQ, dequenched; Q, quenched. **(C and D)** FRET efficiency was measured and plotted. Error bars represent means ± SD. **(E–H)** Statistical quantification of the synaptic recruitment of IgG-BCR and pSyk in J558L cells expressing Mut3– (E), Mut4– (F), Mut5– (G), and Mut6–IgG-BCR (H). Error bars represent means ± SEM. Two-tailed *t* tests were performed for the statistical comparisons. Data are from at least 30 cells over three independent experiments.

of phospholipase C δ (PLCδ) for tracking PI(4,5)P2 (Lemmon et al., 1995; Halet, 2005), Lact-C2 as a PS biosensor (Yeung et al., 2008), Grp1-PH binding domain to indicate PI(3,4,5)P3 (Knight and Falke, 2009), and the 51–91-aa region of Spo20 for probing PA (Kassas et al., 2012; Zhang et al., 2014a). As indicated in Fig. 6 A, only PI(4,5)P2 and not PS, PI(3,4,5)P3, nor PA was enriched in IgG-BCR membrane microdomains in quiescent B cells (Fig. 6, A and B). As further validation, we used a PI(4,5)P2-specific monoclonal antibody to stain PI(4,5)P2 and confirmed that PI(4,5)P2 was enriched in IgG-BCR membrane microdomains in quiescent B cells (Fig. S3 A). We also tested the recruitment of other lipid species such as diacylglycerol (DAG) by using an mEos3.2-fused C1 domain of PKCϑ (Huse et al., 2007), and we found no significant enrichment (Fig. 6, A and B). All these data indicate that the IgG-tail enriches PI(4,5)P2 on the PM in quiescent B cells.

We next tested whether PI(4,5)P2 enrichment was dependent on the PM-tethered status of the IgG-tail by comparing enrichment of the acidic phospholipids within WT, Mut5–, or Mut6–IgG-BCRs. As mentioned above, both Mut5– and Mut6–IgG-BCRs did not tether their IgG-tail to the PM (Fig. 3 D). We found that PI(4,5)P2 enrichment was only obvious in the case of WT IgG-BCRs but not Mut5– nor Mut6–IgG-BCRs (Figs. 6 C and S3 B). We

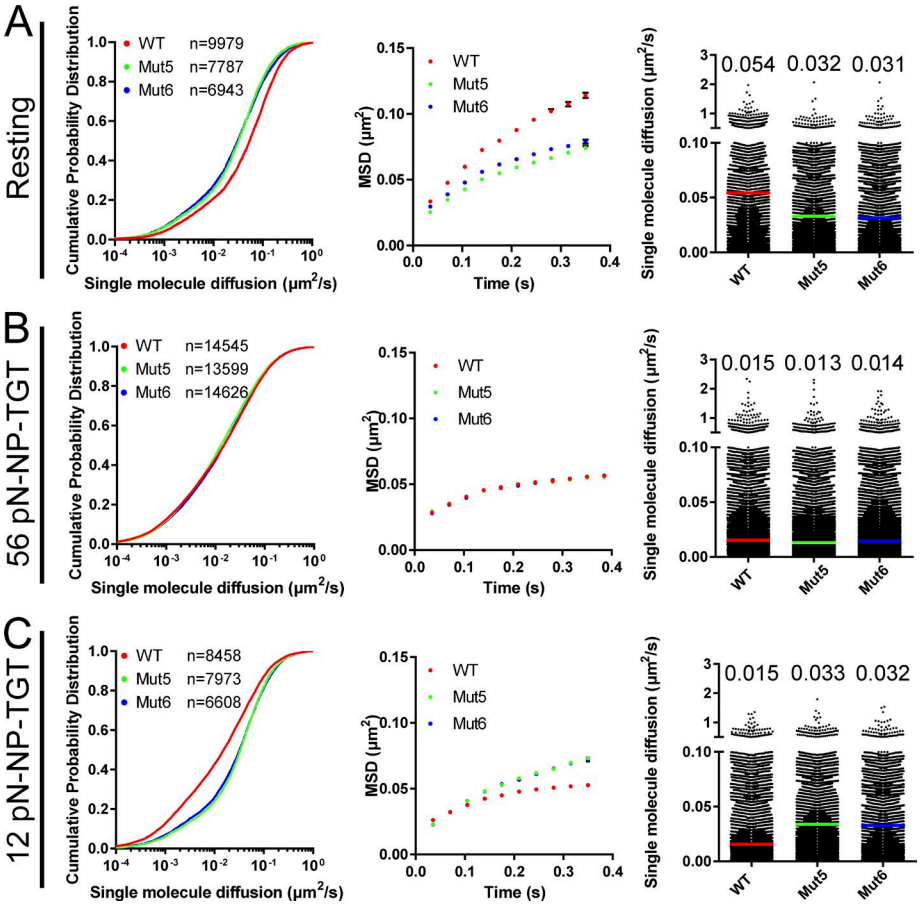

Figure 4. **PM-tethered WT IgG-BCR moves faster at resting stage and slower after encountering 12-pN NP-TGTs in comparison with PM-untethered mutant IgG-BCR, Mut5, and Mut6. (A–C)** A series of mathematical comparisons of the diffusion of WT IgG-BCR, Mut5–IgG-BCR, or Mut6–IgG-BCR molecules in J558L cells at resting stage (A), stimulated with 56 pN NP-TGT (B), or with 12 pN NP-TGT (C) in cumulative probability distribution plots (left), mean square displacement (MSD) plots (middle), or scatter plots (right). Bars represent median values. Data are from at least 30 cells over two independent experiments.

also validated this conclusion through superresolution imaging for both PI(4,5)P2 and IgG-BCR molecules by combining direct stochastic optical reconstruction microscopy (dSTORM) and photoactivated localization microscopy (PALM) technology (Fig. 6 D). Consistently, the results demonstrated that PI(4,5)P2 colocalized better with WT IgG-BCRs than with Mut5– or Mut6–IgG-BCRs (Fig. 6, E–G). All these data indicate that PI(4,5)P2 enrichment at IgG-BCRs is dependent on the PM-tethered status of the IgG-tail. Similarly, we tested the enrichment of PS, PI(3,4,5)P3, PA, and DAG into WT, Mut5–, and Mut6–IgG-BCRs and found no obvious difference (Fig. S3, C–F).

To further characterize the role of positively charged residues in enriching PI(4,5)P2 in the PM-tethered IgG-tail, we measured PI(4,5)P2 enrichment in Mut7 (IgG-tail highly positively charged and PM tethered) at resting stage. Mut7 enriched PI(4,5)P2 similarly to WT IgG-BCR (Fig. 6, H–J). As a negative control, no significant PI(4,5)P2 enrichment was observed in Mut9 (PM tethered but lacking positively charged residues; Fig. 6, K–M). These data indicate that positively charged residues in the PM-tethered IgG-tail are responsible for PI(4,5)P2 enrichment.

Enrichment of PI(4,5)P2 within IgG-BCR membrane microdomains lowers the mechanical force threshold in IgG-BCR activation

The aforementioned results drove us to speculate that PI(4,5)P2 enrichment might be responsible for lowering the mechanical force threshold during the initiation of IgG-BCR activation. To test this hypothesis, we designed a series of experiments to purposely manipulate the amount of PI(4,5)P2 on the PM and then investigated the subsequent effect on the mechanical force threshold of IgG-BCR activation.

First, we evaluated the effect of decreasing the general amount of PI(4,5)P2 on the PM by using a PI(4,5)P2 phosphatase, Ins54p, a 5′ phosphatase from yeast, which dephosphorylates PI(4,5)P2 to produce PI 4-phosphate (Stolz et al., 1998; Raucher et al., 2000; Suh et al., 2006). We also used an Ins54p phosphatase-dead mutant as a negative control. To maximize the efficiency of reducing the amount of PI(4,5)P2 on the PM through Ins54p, we fused the PM-anchoring sequence Lyn16 to the N terminus of Ins54p WT (Lyn16-Ins54p-WT) and the phosphatase-dead control (Lyn16-Ins54p phosphatase-dead control; Fig. 7 A). To quantitatively analyze the amount of PI(4,5)P2 on the PM, we analyzed the ratio of mean fluorescent intensity (MFI) of the PI(4,5)P2-specific fluorescent biosensor (GFP-PH) on the PM versus GFP-PH MFI in the cytosol (Halet, 2005). We observed a marked decrease of the PI(4,5)P2 sensor on the PM in the B cells transfected with Lyn16-Ins54p-WT in comparison with the Lyn16-Ins54p phosphatase-dead control (Fig. 7, B and C). We next tested NP-TGT–triggered activation of WT IgG-BCR–expressing B cells transfected with Lyn16-Ins54p-WT or the phosphatase-dead control. Consistent with our hypothesis, a profound difference was observed between these two types of IgG-B cells: IgG-B cells transfected with Lyn16-Ins54p-WT but not the ones expressing Lyn16-Ins54p phosphatase-dead control failed to maintain the low–mechanical force threshold of IgG-BCR activation (Fig. 7 D).

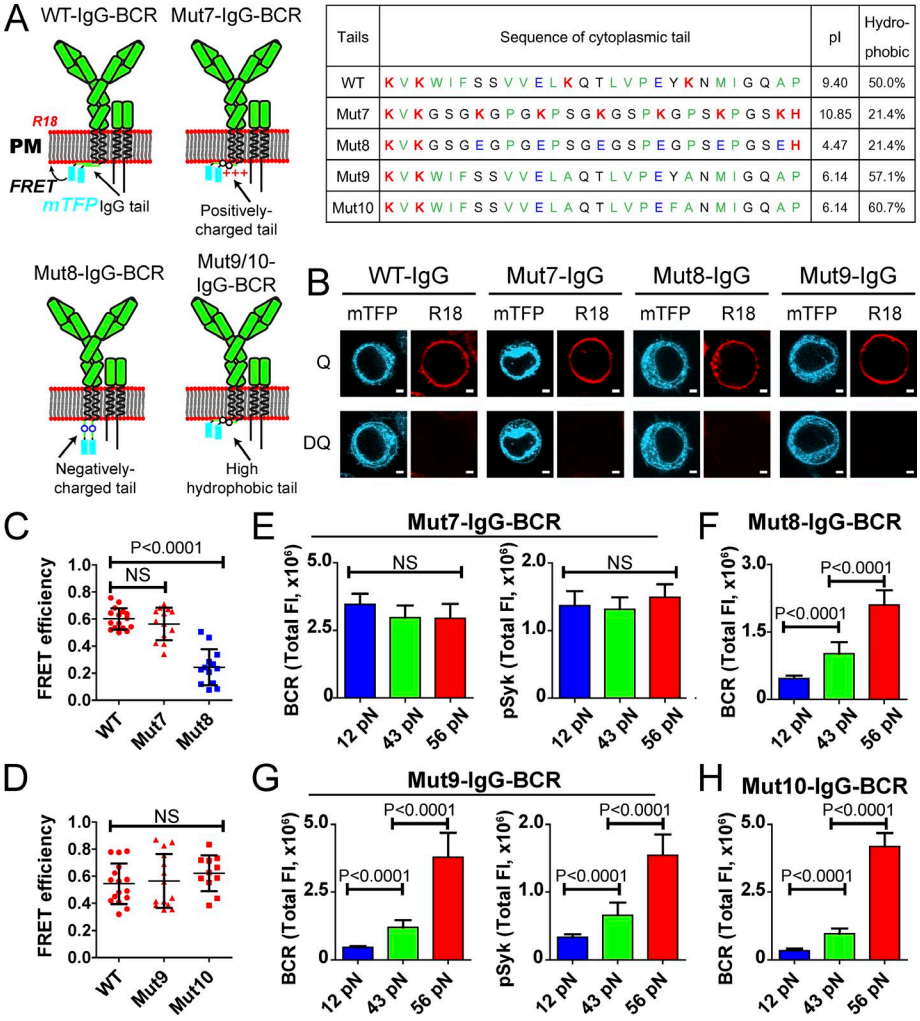

Tails	Sequence of cytoplasmic tail	pI	Hydrophobic
WT	K V K W I F S S V V E L K Q T L V P E Y K N M I G Q A P	9.40	50.0%
Mut7	K V K G S G K G P G K P S G K G S P K G P S K P G S K H	10.85	21.4%
Mut8	K V K G S G E G P G E P S G E G S P E G P S E P G S E H	4.47	21.4%
Mut9	K V K W I F S S V V E L A Q T L V P E Y A N M I G Q A P	6.14	57.1%
Mut10	K V K W I F S S V V E L A Q T L V P E F A N M I G Q A P	6.14	60.7%

Figure 5. **Positively charged residues in the PM-tethered IgG-tail are responsible for the low–mechanical force threshold of IgG-BCR activation. (A)** Left: Schematic illustration showing the FRET system to detect the interaction between mTFP (FRET donor) fused to the C terminus of the cytoplasmic tail (WT and Mut7/8/9/10) and R18 dye (FRET acceptor) stained on the PM. Right: Sequence and biochemical characteristic analysis of the cytoplasmic tail of WT, Mut7 (artificially designed cytoplasmic tail with high pI by high proportion of positively charged residues), Mut8 (artificially designed cytoplasmic tail with low pI as control for Mut7), Mut9, and Mut10 (artificially designed cytoplasmic tail with high hydrophobic level but almost electroneutral). Acidic, basic, and hydrophobic residues are colored in blue, red, and green, respectively. **(B–D)** Dequenching FRET to measure the FRET efficiency between mTFP and R18 in WT, Mut7–, Mut8–, and Mut9–IgG-BCR–expressing DT40 B cells. FRET efficiency was calculated as detailed in Materials and methods. **(B)** Representative confocal images of DT40 B cells expressing WT, Mut7–, Mut8–, and Mut9–IgG-BCR are shown. Bars, 1.1 µm. DQ, dequenched; Q, quenched. **(C and D)** FRET efficiency was measured and plotted. Error bars represent means ± SD. **(E–H)** Statistical quantification for the total FI of accumulated BCRs or pSyk in the immunological synapse of Mut7– (E), Mut8– (F), Mut9– (G), and Mut10–IgG-BCR (H)–expressing J558L cells. Error bars represent means ± SEM. Two-tailed *t* tests were performed for the statistical comparisons. Data are from at least 28 cells over three independent experiments.

To exclude the possibility that the general manipulation of PI(4,5)P2 on the PM might indirectly affect the threshold of IgG-BCR activation by mechanical force, we designed a system to locally manipulate PI(4,5)P2 levels only within IgG-BCR membrane microdomains. Initially, we fused Ins54p to the C terminus of the IgG-tail; however, such chimeric BCRs did not localize to the PM (not depicted). To solve this problem, we took advantage of the rapamycin-based inducible system: rapamycin can simultaneously bind to the FK506 binding protein (FKBP) and FKBP–rapamycin binding (FRB) domains to form a ternary complex (Banaszynski et al., 2005; Suh et al., 2006). Therefore, we fused FKBP with WT Ins54p or Ins54p phosphatase-dead control and the FRB domain with the WT IgG-tail (Fig. 7 E). The WT IgG-tail fused with the FRB domain was well expressed on the PM. After preincubation with rapamycin for 5 min, PI(4,5)P2 enrichment within the WT IgG-BCR–FRB membrane microdomains of B cells expressing FKBP-Ins54p-WT was significantly reduced in comparison with B cells expressing the FKBP-Ins54p phosphatase-dead control (Fig. 7, F and G). Remarkably, WT IgG-BCR–FRB B cells expressing FKBP-Ins54p-WT but not the ones expressing the FKBP-Ins54p phosphatase-dead control failed to maintain the low–mechanical force threshold for IgG-BCR activation (Fig. 7, H and I). As the system control, without rapamycin preincubation treatment, these two cell lines showed no difference on both PI(4,5)P2 enrichment and BCR activation by mechanical force (Fig. S4, A and B). All these results clearly demonstrate that PI(4,5)P2 levels on the PM within IgG-BCR membrane microdomains are of crucial importance for the low–mechanical force threshold in IgG-BCR activation.

Reversely, we examined whether locally increased amounts of PI(4,5)P2 within the membrane microdomains of IgG-BCR mutants with PM-untethered IgG-tails would rescue the loss of the low–mechanical force threshold pattern of these IgG-BCR mutants. We overexpressed in B cells the Lyn16-fused PI 4-phosphate 5-kinase γ (Lyn16-PIP5K), which can potently phosphorylate PI 4-phosphate at the 5-position of the inositol ring to increase the amount of PI(4,5)P2 on the PM. To maximize the efficiency of increasing the amount of PI(4,5)P2 on the PM through Lyn16-PIP5K, we also preincubated B cells with Myo-inositol, a widely used and important component of PI and its various phosphates (Villalobos et al., 2011). Indeed, Myo-inositol preincubation and Lyn16-PIP5K overexpression significantly increased the amount of PI(4,5)P2 in comparison with Myo-inositol preincubation alone or Lyn16-PIP5K overexpression alone (Fig. 8, A–C; and Fig. S4, C–I). Next, we examined the effect of increasing PI(4,5)P2 on the activation of PM-untethered Mut6–IgG-BCR. The results showed that the preincubation of Myo-inositol in combination with the overexpression of Lyn16-PIP5K-WT but

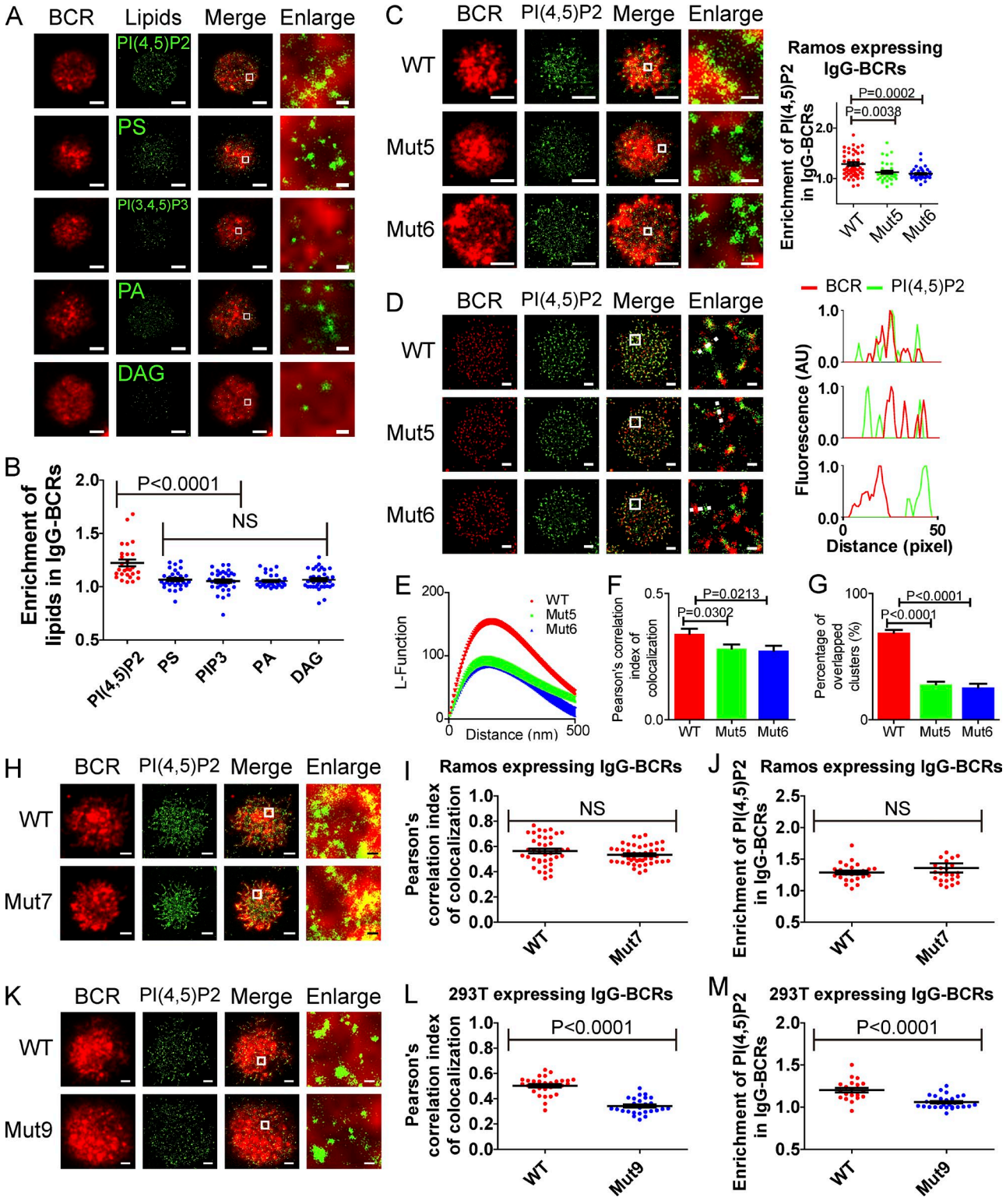

Figure 6. **PI(4,5)P2 is significantly enriched in WT IgG-BCR membrane microdomains in quiescent B cells. (A)** Representative conventional TIRF images of IgG-BCRs and superresolution images of mEos3.2-based lipid biosensors of PI(4,5)P2, PS, PI(3,4,5)P3, PA, and DAG. **(B)** Statistical quantification of enrichment of mEos3.2-based lipid biosensors of PI(4,5)P2, PS, PI(3,4,5)P3, PA, and DAG within WT IgG-BCRs. **(C)** Representative conventional TIRF images of IgG-BCRs and superresolution images of the mEos3.2-based PI(4,5)P2 biosensor within IgG-BCRs of WT, Mut5, and Mut6 in Ramos B cells (left). Statistical quantification of enrichment of mEos3.2-based PI(4,5)P2 biosensor within IgG-BCRs (right). **(D)** Two-color dSTORM and PALM images of BCR labeled with Alexa Fluor 647 goat Fab anti–mouse IgG1 Fc fragment and PI(4,5)P2 labeled with PH-PLCδ-mEos3.2 in Ramos B cells expressing IgG-BCRs with cytoplasmic tail of WT, Mut5, and Mut6. The relative fluorescence intensity distributions of BCR (red) and PI(4,5)P2 (green) along the white dashed lines are shown on the right. **(E–G)** L-function (E), Pearson correlation index analyses (F), and percentages of overlapped clusters (G) were used to quantify the spatial distribution of BCR with PI(4,5)P2 in Ramos B cells expressing IgG-BCRs with cytoplasmic tail of WT, Mut5, and Mut6 in quiescent B cells. **(H)** Representative conventional TIRF images of IgG-BCRs

not the Lyn16-PIP5K kinase-dead control rescued the mechanical force threshold for the activation of Mut6–IgG-BCR (Fig. 8 D). As a further test, we also similarly increased the amount of PI(4,5)P2 on the PM of B cells expressing IgM-BCRs and found that such treatment lowered the mechanical force threshold of IgM-BCRs (Figs. 8 E and S4 H).

We again took advantage of the rapamycin-based inducible system to locally manipulate PI(4,5)P2 levels only within IgG-BCR membrane microdomains. In brief, FKBP was fused with PIP5K-WT or the PIP5K kinase-dead control, and the FRB domain was fused with Mut6–IgG-tail. After preincubation of Myo-inositol for 1 h and rapamycin for 5 min, PI(4,5)P2 enrichment within Mut6–IgG-BCR–FRB membrane microdomains of B cells expressing FKBP-PIP5K-WT was significantly increased in comparison with B cells expressing the FKBP-PIP5K kinase-dead control (Fig. 8, F-H). Mut6–IgG-BCR–FRB B cells expressing FKBP-PIP5K-WT but not the ones expressing the FKBP-PIP5K kinase-dead control significantly lowered the mechanical force threshold of IgG-BCR activation (Fig. 8, I and J). As the system control, without rapamycin preincubation treatment, these two cell lines showed no difference on both PI(4,5)P2 enrichment and BCR activation by mechanical force (Fig. S4, J and K). Thus, all these data indicate that enrichment of PI(4,5)P2 within IgG-BCR membrane microdomains is both required and sufficient to lower the mechanical force threshold during the initiation of IgG-BCR activation (see also Fig. 9).

Discussion

This study reported that the low–mechanical force threshold of IgG-BCR activation depends on the PM-tethered state of the IgG-tail in quiescent B cells. Moreover, positively charged residues in PM-tethered IgG-tail are crucial for recruiting PI(4,5)P2 within IgG-BCR membrane microdomains and consequently maintain the low–mechanical force threshold of IgG-BCR activation. Manipulating the amounts of PI(4,5)P2 within IgG-BCR membrane microdomains drastically changes the thresholds of mechanical force–induced B cell activation. Our study sheds light on an IgG-tail–mediated PI(4,5)P2 enrichment–dependent mechanism that lowers the mechanical force threshold of IgG-BCR activation. All these findings highlight a novel explanation on the low force requirement to initiate the activation of IgG-BCR in memory B cells and imply a new mechanism to explain the rapid IgG antibody responses of memory B cells upon reencountering antigens.

Our study used the dsDNA-based TGT system that was originally developed by Wang and Ha (2013). Because the minimum rupture force value of TGTs is ∼12 pN, it will be interesting to take other approaches (Zhang et al., 2014b; Chowdhury et al., 2016) to test how the mechanical force <12 pN would induce IgG-BCR activation. Moreover, the TGT system cannot be applied to measure the dynamic changes of mechanical forces exerted through BCR structures during antigen recognition because its rupture is irreversible. Thus, future studies using the nonrupturable tension sensors will also be required (Liu et al., 2016b; Nowosad et al., 2016; Spillane and Tolar, 2017). In our experiments, we used the Ramos human B cell line, J558L/CH27 mouse B cell line, and DT40 chicken B cell line. We chose to use these different types of B cells for certain reasons: (A) it is required to ensure that the conclusion is of general meanings but is not limited to a certain type of B cells; (B) there is no single type of B cell that can fulfill the purpose of all the experiments in our manuscript. Moreover, we expressed the species-matched BCRs or the complete BCR complex in these cell lines to ensure the proper BCR expression and the following experiments. For example, we expressed the BCRs with human constant regions to Ramos human B cell lines, the BCRs with mouse constant regions to J558L/CH27 mouse B cell lines, and the whole complex of mouse BCRs to DT40 and 293T cell lines.

Our study demonstrates that PI(4,5)P2 enrichment in IgG-BCR membrane microdomains is vital for IgG-BCR activation by low mechanical force; however, we cannot rule out the contributions of other phospholipids such as PI, which has the largest number of negatively charged lipid species on the PM. According to our knowledge, there unfortunately is no well-developed PI biosensor with high specificity. Besides, our study shows that PI(3,4,5)P3 is not significantly enriched in IgG-BCR membrane microdomains compared with PI(4,5)P2 at resting stage. Such an observation is unexpected because PI(3,4,5)P3 is more negatively charged than PI(4,5)P2 at physiological conditions, and theoretically, PI(3,4,5)P3 would be more attracted by positively charged residues in IgG-tail. We suspect that such a phenomenon is because the total amount of PI(3,4,5)P3 is much less than that of PI(4,5)P2 on the PM. In this study, we found that at the physiological conditions of a B cell, PI(4,5)P2 enrichment by positively charged residues of PM-tethered cytoplasmic tail determines the mechanical force threshold of IgG-BCR activation. In marked contrast, at the nonphysiological condition, when B cells have artificially increased the total amount of PI(4,5)P2 on the PM by the overexpression of Lyn16-PIP5K and the preincubation with Myo-inositol, the amount of PI(4,5)P2 within Mut6–IgG-BCR membrane microdomains increased because there was overall more PI(4,5)P2 on the PM. In this nonphysiological condition, Mut6–IgG-BCR and IgM-BCR exhibited the low–mechanical force threshold in response to NP-TGTs, indicating that with too much PI(4,5)P2 on the PM, the function of PI(4,5)P2 in the force sensitivity profile is not necessary through direct interaction with IgG-tail.

and superresolution images of mEos3.2-based lipid biosensors of PI(4,5)P2 in Ramos B cells expressing IgG-BCRs with cytoplasmic tails of WT or Mut7. **(I and J)** Pearson's correlation index analyses (I) and enrichment analyses (J) were used to quantify the spatial distribution of BCR with PI(4,5)P2 in Ramos B cells expressing IgG-BCRs with cytoplasmic tails of WT and Mut7 in quiescent states. **(K)** Representative conventional TIRF images of IgG-BCRs and superresolution images of mEos3.2-based lipid biosensors of PI(4,5)P2 in 293T cells expressing IgG-BCRs with cytoplasmic tails of WT or Mut9. Enlarged images are marked by white squares in main images. Bars: (A, main images) 4 µm; (A, enlarged images) 320 nm; (C, D, H, and K, main images) 2 µm; (C, D, H, and K, enlarged images) 200 nm. **(L and M)** Pearson's correlation index analyses (L) and enrichment analyses (M) were used to quantify the spatial distribution of BCR with PI(4,5)P2 in 293T cells expressing IgG-BCRs with cytoplasmic tails of WT and Mut9 in quiescent B cells. Error bars represent means ± SEM. Two-tailed *t* tests were performed for statistical comparisons. Data are from at least 25 cells over two independent experiments.

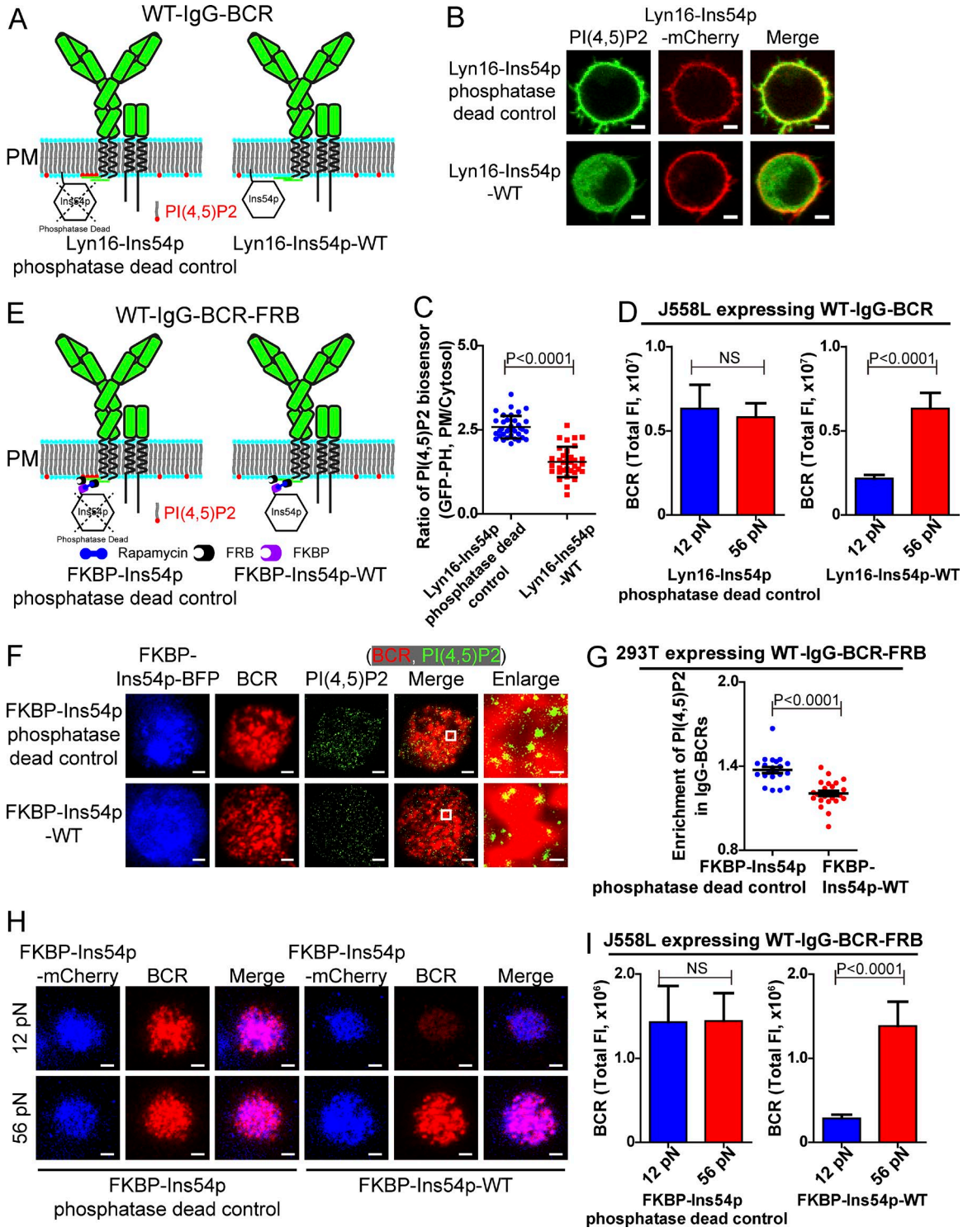

Figure 7. **Depletion of PI(4,5)P2 within IgG-BCR membrane microdomains increases the mechanical force threshold in IgG-BCR activation. (A)** A schematic diagram depicting the PI(4,5)P2 depletion through membrane-anchored Ins54p in B cells expressing WT IgG-BCRs. Phosphatase-dead Ins54p (named Lyn16-Ins54p phosphatase-dead control) was used as control for WT Ins54p (named Lyn16-Ins54p-WT). **(B)** Representative confocal images of PI(4,5)P2 lipid biosensor (GFP-PH) and Lyn-Ins54p-mCherry on DT40 B cell membrane are shown. **(C)** Statistical quantification of the ratio of MFI of GFP-PH on the PM versus MFI of GFP-PH in cytosol of DT40 B cells expressing Lyn-Ins54p phosphatase-dead control or Lyn16-Ins54p-WT. Error bars represent means ± SD. **(D)** Statistical quantification of the synaptic accumulation of WT IgG-BCR of J558L cells expressing Lyn16-Ins54p phosphatase-dead control or Lyn16-Ins54p-WT encountering 12-pN or 56-pN NP-TGT sensors. **(E)** A schematic diagram depicting the PI(4,5)P2 depletion within membrane microdomains of WT IgG-BCR through a rapamycin-based inducible system of WT IgG-BCR–FRB and FKBP-Ins54p-WT. Phosphatase-dead Ins54p (named FKBP-Ins54p phosphatase-dead control) was used as control for FKBP-Ins54p-WT. **(F)** Representative conventional TIRF images of FKBP-Ins54p-BFP, WT IgG-BCRs, and superresolution images of mEos3.2-based lipid biosensors of PI(4,5)P2 in 293T cells expressing FKBP-Ins54p-WT or FKBP-Ins54p phosphatase-dead controls after preincubation with rapamycin for 5 min. **(G)** Statistical quantification of enrichment of mEos3.2-based PI(4,5)P2 biosensor within WT IgG-BCR membrane microdomains. **(H)** Representative TIR

PI(4,5)P2 may facilitate and direct BCR accumulation into immunological synapses when B cells are stimulated by low mechanical forces and also may provide directionality and contextual cues for downstream signaling to boost IgG B cell activation in several aspects: First of all, it is known that PI(4,5)P2 is one of the key lipid species managing the cytoskeleton system through regulating PI(4,5)P2-binding proteins such as N-WASP (Miki et al., 1996), Cdc42 (Burbage et al., 2015), the ezrin, radizin, and moesin family (Treanor et al., 2011), vinculin, talin, gelsolin, profilin, and other key regulators (Czech, 2000; Logan and Mandato, 2006). Second, the enrichment of PI(4,5)P2 within IgG-BCR membrane microdomains increases the PI(4,5)P2 accessibilities for other PI(4,5)P2-binding proteins, especially enzymes such as PI 3-kinase, PLC, and phospholipase D (McLaughlin et al., 2002; Hikida et al., 2009; Xu et al., 2015; Petersen et al., 2016), to amplify the weak signals initiated by the low mechanical force to further activate downstream signalosomes through PI(3,4,5)P3, IP3/Ca^{2+}, or PA, respectively.

The cytoskeleton controls the mobility of BCRs and the formation of BCR microclusters during the initiation of B cell activation (Tolar et al., 2009; Liu et al., 2010a; Treanor et al., 2010, 2011; Schnyder et al., 2011; Davey and Pierce, 2012; Natkanski et al., 2013; Wang et al., 2016). When BCRs are activated by lipid bilayer–presenting antigens, the mobility of BCRs will be reduced concomitant with F-actin remodeling, BCR oligomerization, and the formation of BCR microclusters, all of which work concertedly to promote B cell activation (Tolar et al., 2009; Liu et al., 2010a,b). Indeed, our study showed that in conditions lacking PI(4,5)P2 enrichment within the PM-untethered mutant IgG-BCR membrane microdomains, the movement of these mutant IgG-BCRs cannot consistently slow down when activated by 12-pN NP-TGTs; however, PI(4,5)P2-enriched WT IgG-BCR can significantly reduce its mobility on 12-pN NP-TGTs, implying a sophisticated mobility regulation system through IgG-tail–enriched PI(4,5)P2. Additionally, related to BCR mobility, our study shows that WT IgG-BCRs diffuse faster than PM-untethered mutant IgG-BCRs at the resting stage but move slower than PM-untethered mutant IgG-BCRs when encountering 12-pN NP-TGTs. All these observations inspire us to hypothesize that the rupture forces that can be exerted by the energies from BCR mobility could be likely contributed as a sum by the factors including the oligomerization of BCRs, the heterogeneity of lipid species, membrane bending (curvature), cytoskeletons, motor proteins, et cetera. Moreover, the kinetic energy changes from fast mobility to slow movement might be also transformed to other types of energy such as elastic potential energy from BCR conformational change or cytoskeleton-shaping tension to initiate BCR activation signaling.

The enrichment of negatively charged lipid species by the positively charged juxtamembrane region at the resting stage has also been found in epidermal growth factor receptor, in which PI(4,5)P2 enrichment controls the clustering of epidermal growth factor receptor in quiescent state, further regulating downstream activation (Wang et al., 2014). This study showed that the value of PI(4,5)P2 enrichment within IgG-BCR membrane microdomains is ∼1.3, which is similar to the value of IgM-BCR within Syk microclusters (∼1.5; Mattila et al., 2013) but is not as dramatically high as the value of FcγRIIB enrichment in immune complex microclusters (∼3.0; Xu et al., 2016), indicating that potentially there are other membrane proteins or proteins located in membrane-proximal region in B cells regulating the PI(4,5)P2 distribution on the PM. We speculate that there might be a PI(4,5)P2-mediated orchestration system coordinately regulating different membrane-bound proteins and signal proteins to initiate activation of B cells that is yet to be discovered.

IgG mutants—which cannot recruit PI(4,5)P2 around IgG-BCR membrane microdomains at the resting stage—such as Mut5, get activated by mechanical force in the same multithreshold matter as IgM-BCRs. We speculate that IgM- and IgG-BCR may share the same force-transduction components. The antigenic signal needs to be delivered from the antigen-binding region on the extracellular domain of IgM/IgG-BCR to the signaling active immunoreceptor tyrosine–based activation motif on the cytoplasmic domain of both Igα and Igβ. However, the mechanism is still enigmatic. Because antigen binding–induced formation of BCR microclusters relies on conformational change of BCR heavy chain (Tolar et al., 2009), we speculate that mechanical force–induced BCR activation may also depend on conformational change to transduce force to chemical signals, similar to TCR (Kim et al., 2009; Huang et al., 2010; Liu et al., 2014; Lee et al., 2015; Dustin and Kam, 2016). Moreover, we speculate that Igα and Igβ may play different roles in the mechanical force transduction process, providing two distinct signaling pathways resulting in multiple mechanical force thresholds of activation as implied by Lee and Tolar (2013) that cytoplasmic domain of Igα increases membrane proximity after stimulation but not Igβ. All these speculations are under our further extensive investigation.

In summary, the findings presented in this study indicate a mechanism for mechanical force induced more sensitive activation of IgG-BCR–expressing memory B cells. Such a mechanism is achieved by the enrichment of the vital signaling transduction phospholipid PI(4,5)P2 through PM-tethered positively charged IgG-tail in quiescent B cells to boost IgG-BCR activation in a low–mechanical force threshold manner. Our study may have far-reaching implications on vaccine development and design and offers fresh prospects for explanation of rapid memory B cell activation.

FM images of FKBP-Ins54p-mCherry or BCRs in J558L cells expressing either FKBP-Ins54p-WT or FKBP-Ins54p phosphatase-dead control when encountering 12-pN or 56-pN NP-TGTs. Enlarged images in F are marked by white squares in main images. Bars: (B, F [main images], and H) 2 µm; (F, enlarged images) 200 nm. **(I)** Quantification of the total FI of BCR accumulation into immunological synapses in contact with the surfaces of 12-pN or 56-pN NP-TGTs. Error bars represent means ± SEM. Two-tailed *t* tests were performed for the statistical comparisons. Data are from at least 20 cells over two independent experiments, except as specifically described.

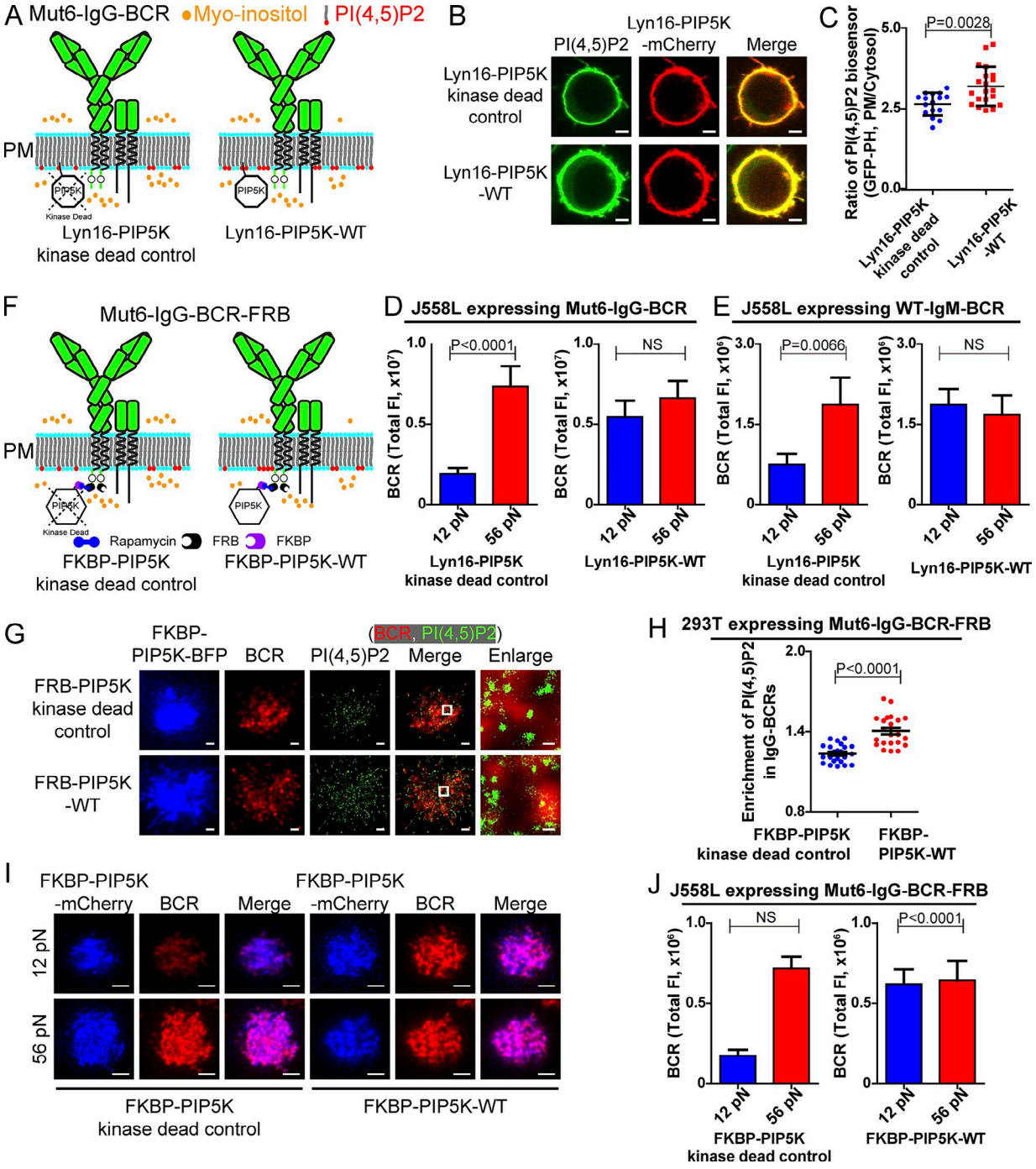

Figure 8. **Enrichment of PI(4,5)P2 within IgG-BCR membrane microdomains lowers the mechanical force threshold in IgG-BCR activation. (A)** Schematic representation showing the amount of PI(4,5)P2 increasing through membrane-anchored PIP5K in B cells expressing Mut6–IgG-BCRs. Kinase-dead PIP5K (named Lyn16-PIP5K kinase-dead control) was used as control for WT PIP5K (named Lyn16-PIP5K-WT). **(B)** Representative confocal images of PI(4,5)P2 sensor (GFP-PH) and Lyn-PIP5K-mCherry on DT40 B cell membrane are shown. **(C)** Statistical quantification of ratio of MFI of GFP-PH on the PM versus the MFI of GFP-PH in the cytosol of DT40 B cells expressing Lyn-PIP5K kinase-dead control or Lyn16-PIP5K-WT. Error bars represent means ± SD. **(D and E)** Statistical quantifications of the synaptic accumulation of Mut6–IgG-BCR (D) or WT IgM-BCR (E) of J558L cells expressing Lyn16-PIP5K kinase-dead control or Lyn16-PIP5K-WT encountering 12-pN or 56-pN NP-TGT sensors. **(F)** A schematic diagram depicting the PI(4,5)P2-increasing system within membrane microdomains of Mut6–IgG-BCR through a rapamycin-based inducible system of Mut6–IgG-BCR–FRB and FKBP-PIP5K-WT. Kinase-dead PIP5K (named FKBP-PIP5K kinase-dead control) was used as control for FKBP-PIP5K-WT. **(G)** Representative conventional TIRF images of FKBP-PIP5K-BFP and Mut6–IgG-BCRs and superresolution images of mEos3.2-based lipid biosensors of PI(4,5)P2 in 293T cells expressing FKBP-PIP5K-WT or FKBP-PIP5K kinase-dead control after preincubation with rapamycin for 5 min. **(H)** Statistical quantification of enrichment of mEos3.2-based PI(4,5)P2 biosensor within Mut6–IgG-BCRs. **(I)** Representative TIRFM images of FKBP-PIP5K-mCherry or Mut6–IgG-BCRs in J558L cells expressing either FKBP-PIP5K-WT or FKBP-PIPK5 kinase-dead control when encountering 12-pN or 56-pN NP-TGTs. In G, enlarged areas are marked by white squares in main images. Bars: (B, G [main images], and I) 2 µm; (G, enlarged images) 200 nm. **(J)** Quantification of the total FI of BCR accumulation into immunological synapses in contact with surfaces of 12-pN or 56-pN NP-TGTs. Error bars represent means ± SEM. Two-tailed *t* tests were performed for the statistical comparisons. Data are from at least 20 cells over two independent experiments except specific descriptions.

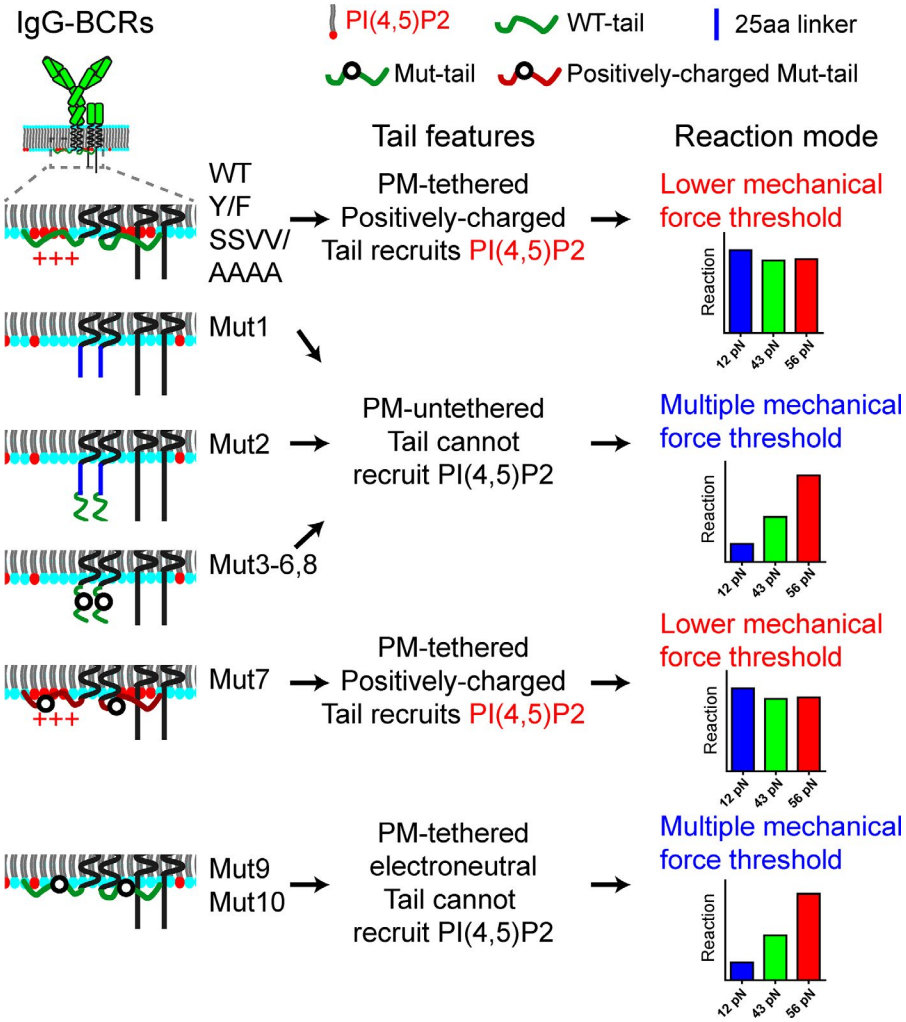

Figure 9. **Schematic diagram of all the tails tested in this study.** Cartoon models indicating characteristics and activation features of all cytoplasmic domains tested in this study.

Materials and methods

Plasmids

Mouse B1-8–specific WT IgG-tail–mTFP plasmid was used as described previously (Chen et al., 2015). In brief, a monomeric version of TFP was attached to the C termini of mouse NP-specific B1-8 IgG heavy chains constructed in a pHAGE backbone. All the mutant cytoplasmic tail vectors were constructed based on the WT version in pHAGE backbone. Human B1-8–specific IgG-, IgM-, and IgE-heavy chain plasmids were constructed as described in our previous study (Wan et al., 2015). In short, human IgG-, IgM-, IgE-, IgA-, and IgD-constant regions of heavy chains were fused with a B1-8–specific variable region at the N terminus and with mTFP at the C terminus to construct B1-8–specific heavy chains. The plasmid of the human version of the B1-8–specific light chain was constructed by fusing the B1-8–variable region to the N terminus of the human Igλ-constant region. The cDNA mEos3.2 was a gift from P. Xu and T. Xu (Institute of Biophysics, Beijing, China); the plasmid PIP5Kγ87 was a gift from P. De Camilli (Yale University, New Haven, CT; 22300; Addgene); and CP-Ins54p, CP-Ins54p phosphatase-dead mutant (D281A), Lyn11-targeted FRB, and GFP-C1-PLCδ-PH were gifts from T. Meyer (Stanford University, Stanford, CA; 20155, 20156, 20147, and 21179, respectively; Addgene). PM-anchoring Ins54p-WT or phosphatase-dead mutant (D281A) and PIP5K-WT or kinase-dead mutant were constructed by fusing the membrane-anchoring sequence Lyn16 to the N terminus of these plasmids. BFP/mCherry-FKBP-Ins54p and BFP/mCherry-FKBP-Ins54p phosphatase-dead control plasmids were constructed based on CF-Ins54p and CF-Ins54p (D281A). FKBP fragment was fused to the PIP5K-WT or PIP5K kinase-dead mutant (D253A) to construct FKBP-PIP5K-WT or FKBP-PIP5K kinase-dead control. All PIP5K constructs used in this study were based on a mutant version of PIP5Kγ with R445E, K446E, and S264A substitutions to prevent its intrinsic PM localization (Suh et al., 2006). The FRB fragment was cloned from Lyn11-targeted FRB and fused to the C terminus of the WT- or Mut6–cytoplasmic tail of IgG-tail. All these plasmid construction, point mutations, and truncations were performed following Gibson assembly protocol (Gibson et al., 2009).

Cells, antigens, antibodies, and reagents

Mouse J558L cells, CH27, and human Ramos B cells were cultured in RPMI 1640 medium containing 10% FBS, penicillin, and streptomycin antibiotics (Invitrogen) as described previously (Liu et al., 2010c; Sohn et al., 2011). All these B cell lines were gifts from S.K. Pierce (National Institutes of Health, Bethesda, MD). DT40 B cells (Takata et al., 1995) were gifts for laboratory studies from T. Kurosaki (Institute of Physical and Chemical Research, Yokohama, Japan). DT40 B cells were cultured in RPMI 1640 medium

containing 10% FBS, 1% chicken serum, 50 µM 2-mercaptoethanol, penicillin, and streptomycin antibiotics (Thermo Fisher Scientific) as described previously (Ishiai et al., 1999; Weber et al., 2008). 293T cells were cultured in DMEM containing 10% FBS, penicillin, and streptomycin antibiotics. Mouse J558L cells stably expressing Igα-YFP were constructed and maintained as previously described (Liu et al., 2010a) and further transfected with IgG–heavy chain of WT or mutant cytoplasmic tails. 293T or DT40 cells were transiently transfected with light chain, Igα, Igβ, and heavy chain of WT or each mutant cytoplasmic tail to assemble intact IgG-BCRs by calcium phosphate transfection or electroporation (Lonza), respectively. Ramos B cells were transfected with B1-8–specific human light chain and heavy chain of IgM-, IgD-, IgA-, IgG-, or IgE-BCR to test the mechanical force threshold of diverse types of BCR activation. Ramos B cells were transfected with WT or mutant IgG–heavy chain and mEos3.2-PH to detect the PI(4,5)P2 enrichments. CH27 B cells were transfected with WT or mutant IgG–heavy chain and mEos3.2-fused Lact-C2, Grp1-PH, and the 51–91-aa region of Spo20 for probing PA to detect the enrichments of PS, PI(3,4,5)P3, and PA in IgG-BCR membrane microdomains, respectively.

Alexa Fluor 647 or Cy3 AffiniPure Fab fragment goat anti–mouse IgG1 Fc fragment specific and Cy5-Fab fragment goat anti–mouse IgM µ chain specific (Jackson ImmunoResearch Laboratories, Inc.) were used for mouse IgG- and IgM-BCR cell surface staining, respectively. Alexa Fluor 647 AffiniPure Fab fragment goat anti–human IgG Fcγ fragment specific (Jackson ImmunoResearch Laboratories, Inc.) was used for human IgG-BCR cell surface staining. In short, the cells were stained with 100 nM antibody on ice for 10 min. After washing three times with PBS, the cells were ready for further experiments. Myo-inositol was purchased from Sigma-Aldrich. Rapamycin was a gift from Y. Zhang (Tsinghua University, Beijing, China).

BCR expression level

J558L and DT40 B cell lines expressing WT or each mutant IgG-BCR were tested for both PM expression and total expression by flow cytometry (Accuri C6; BD). In detail, to test the BCR expression on the PM, intact B cells were stained with 100 nM Alexa Fluor 647 Fab fragment goat anti–mouse IgG1 Fc fragment specific on ice for 10 min; afterward, cells were washed twice with PBS and were ready to examine under flow cytometry. To examine the total expression of BCRs, B cells were fixed by 4% PFA for 30 min. After washing twice with PBS, the B cells were permeabilized with 0.1% Triton X-100 and then stained with Alexa Fluor 647 Fab fragment goat anti–mouse IgG1 Fc fragment specific for 30 min. After washing three times with PBS, cells were ready for flow cytometry examination.

Preparation of B1-8 NP-TGTs

NP-TGTs were prepared by following the published protocol (Wang and Ha, 2013) with some modifications. In detail, we conjugated NP hapten to one DNA strand (ssDNA) of the dsDNA of TGTs to specifically activate B cells. NP-e-aminocaproyl-OSu (Biosearch Technologies) were conjugated to ssDNA with NH2 group modification. The sequence used was 5′-CACAGCACGGAG GCACGACAC-NH2/-3′.

The other strand of the TGT had a biotin tag at a predesigned position for performing different rupture force points and binding to the coverslip through a biotin-neutravidin bond. The sequence used was 5′-GTGTCGTGCCTCCGTGCTGTG-3′ with the biotin label at the first, 11th, and 21st bases, which formed 12, 43, and 56 pN, respectively. NP-ssDNA and biotin-ssDNA were further annealed in the annealing buffer following the protocol from Invitrogen.

Coverslips (VWR International) were pretreated with stripping buffer (7:3 H_2SO_4/H_2O_2), washed, and dried. Then, dried coverslips were attached to the disposable eight-well chamber frame (Lab-Tek chambers; Nunc) or a home-designed microchamber with glue. Each well of microchamber had a diameter of 2.5 mm. After 20 min of curing at RT, chamber was ready to use for downstream experiment. 200 µg/ml neutravidin was added to the coverslip, and after incubation for 30 min at 37°C, extensive washing was performed. NP-TGTs were then loaded to the coverslip at the concentration of 50 nM for 30 min at RT for the purpose of tethering NP-TGTs to the coverslip. After careful washing with PBS, the coverslip was blocked with 1% casein (wt/vol) in PBS for 30 min at 37°C. After washing again with PBS, the NP-TGT–conjugated coverslip was ready for further use. The prestained cells were then loaded on the surface for reaction at 37°C for 10 min if there were no specific indications.

Molecular imaging by TIRFM and confocal fluorescence microscopy

TIRFM images were acquired by an Olympus IX-81 microscope equipped with a TIRF port, an Andor iXon$^+$ DU-897D electron-multiplying charge-coupled device camera, and an Olympus 100× 1.49 NA objective lens. The acquisition was controlled by MetaMorph software (Molecular Devices). For the imaging options, the exposure time was 100 ms for a 512 × 512–pixel image unless specially indicated. Confocal images were acquired by a FLUOVIEW FV1000 confocal laser scanning microscope (Olympus) with a 60× 1.42 NA oil objective lens. All the images were acquired while keeping the cells in PBS unless specially indicated and were confirmed not to overexpose by the software. All the images were analyzed and processed with ImageJ (National Institutes of Health). The MFI and the total fluorescence intensity (total FI) as AU of BCRs, lipid biosensors, and signaling molecules were calculated based on the intensity analysis as described previously (Lakadamyali et al., 2004; Liu et al., 2010b,c, 2012).

FRET measurement

To perform the FRET experiments, 1 × 10^6 cells were collected and washed once with 1× PBS and then suspended in 1 ml cell buffer. Before loading to the poly-L-lysine (Sigma-Aldrich)–coated chambered coverglass slides (Thermo Fisher Scientific), 300 µl aliquots of cells were stained with 300 nM octadecyl rhodamine B (R18; Invitrogen) on ice for 3 min. The chamber was then mounted onto an FV1000 microscope and maintained for 5 min to allow cell adhesion. Dequenching FRET images were captured (Xu et al., 2008; Shi et al., 2013; Chen et al., 2015). mTFP was excited with a 473-nm laser and visualized using a 520/40 bandpass filter. R18 was excited with a 559-nm laser line and visualized using the 625/100 bandpass filter. All the FRET

experiments were performed in Ringer's buffer with 2 mM Ca^{2+} and 1 mM Mg^{2+}. The images of same cells on both mTFP and R18 channels were acquired before and after bleaching the acceptor (R18) by a 559-nm laser to dequench the donor (mTFP). All the images were processed with ImageJ, and the MFI of IgG-BCRs only expressed on the PM was quantified by using region of interest tools in ImageJ. FRET efficiency was calculated with the formula FRET efficiency = (DQ − Q)/DQ, with DQ and Q representing dequenched and quenched donor fluorescence intensity (mTFP), respectively.

Intracellular immunofluorescence staining and molecular imaging

The recruitment of signaling molecules into the immunological synapse of B cells stimulated by NP-TGTs was imaged by TIRFM by following our previously published protocol (Liu et al., 2010a,b,c, 2012). In brief, BCRs expressed on the PM were prestained with fluorescent dye labeled with Fab antibody as described in the Cells, antigens, antibodies, and reagents section. Then, B cells were loaded to the chambered coverglasses to react with NP-TGTs for 10 min followed by 4% PFA fixation for 30 min. After washing with 10 ml PBS, the B cells were permeabilized with 0.1% Triton X-100 and then blocked with 100 µg/ml goat nonspecific IgG (Jackson ImmunoResearch Laboratories, Inc.). Subsequently, cells were stained with phospho–Zap-70(Tyr319)/Syk (Tyr352) primary antibody (Cell Signaling Technology) at 37°C for 1 h. After washing with 10 ml PBS, B cells were stained with secondary antibody Alexa Fluor 568–conjugated $F(ab')_2$ goat antibody specific for rabbit or mouse IgG (Invitrogen) as previously described (Liu et al., 2012). PI(4,5)P2 intracellular staining was performed by following a protocol provided by Echelon Biosciences Inc. In brief, 293T cells expressing human WT IgG-BCRs were fixed using 4% PFA (wt/vol), permeabilized with 0.5% saponin (Sigma-Aldrich), blocked by 10% goat serum and 2.5% BSA, and then incubated by 10 µg/ml anti-PI(4,5)P2 monoclonal antibody (Z-P045; Echelon Biosciences Inc.) at 37°C. After washing, the cells were stained with a second antibody, Cy3-conjugated $F(ab')_2$ goat anti–mouse IgM, at a concentration of 2 µg/ml. In downstream activation tests, J558L cells expressing WT IgM- or WT IgG-BCRs were rested in RPMI 1640 culture media for 30 min before being loaded onto the NP-TGT–coated coverglasses. After 10 min of incubation, cells were fixed by 4% PFA, permeabilized with cold methanol, blocked with 10% goat serum, and sequentially stained with the anti-pERK antibody (AF1018; R&D Systems), an Alexa Fluor 647–conjugated $F(ab')_2$ goat anti–rabbit IgG (Invitrogen), and a nucleic acid dye Hoechst. After washing with PBS, the cells were imaged by fluorescence microscopy (Su et al., 2016). Images were analyzed by ImageJ following our published protocols (Liu et al., 2010a,b,c, 2012).

Treatment of B cells with Myo-inositol

For increasing PI(4,5)P2 studies, DT40, or J558L, B cells expressing either Lyn16-PIP5K kinase-dead control or Lyn16-PIP5K-WT were pretreated with Myo-inositol (Sigma-Aldrich) in 1 mM at cell culture conditions for 1 h before the imaging experiment (Villalobos et al., 2011).

Superresolution imaging and analysis

To acquire the PALM images of PI(4,5)P2, PS, PI(3,4,5)P3, PA, and DAG at resting stage, specified cells respectively expressing mEos3.2-fused PLCδ-PH (Lemmon et al., 1995; Halet, 2005), Lact-C2 (Yeung et al., 2008), Grp1-PH (Knight and Falke, 2009), the 51–91-aa region of Spo20 (Kassas et al., 2012; Zhang et al., 2014a), or C1-PKCϑ (Huse et al., 2007) were placed on poly-L-lysine– or fibronectin-coated coverglasses and fixed with 4% PFA at 10 min. Stream videos were acquired by 561-nm laser (10 mW) irradiation at a recording rate of 30 frames per second simultaneously with a continuous low-power 405-nm laser to convert a small portion of mEos3.2 from green to red to generate single molecular signals. Image registration and drift correction were achieved by the position of fluorescent microspheres (100 nm TetraSpek; Thermo Fisher Scientific). For analysis of PALM images, peaks of single points were first identified by using Insight3 software provided by X. Zhuang (Harvard University, Cambridge, MA), B. Huang (University of California, San Francisco, San Francisco, CA), and Y. Sun (Peking University, Beijing, China). Enrichment of PI(4,5)P2, PS, PI(3,4,5)P3, PA, and DAG inside BCRs was measured using the MATLAB (MathWorks) codes written according to the algorithms reported previously (Zhang et al., 2006; Owen et al., 2010; Mattila et al., 2013). In detail, the enrichment of lipid molecules within IgG-BCR membrane domains was analyzed in a rectangular window of 3 µm side length around the center of the cells, and we calculated the enrichment of lipid molecules within IgG-BCR membrane domains as the fraction of localized lipid molecules residing in IgG-BCR membrane domains divided by the fraction of the area occupied by IgG-BCR membrane microdomains.

dSTORM technology was used for superresolution imaging of IgG-BCRs. Alexa Fluor 647–conjugated AffiniPure Fab fragment goat anti–mouse IgG1 Fc fragment specific was used to stain IgG-BCRs for two-color superresolution imaging of BCR and PI(4,5)P2. Before imaging, fixation buffer was washed, and imaging buffer (containing 140 mM β-mercaptoethanol, 0.5 mg/ml glucose oxidase, and 40 µg/ml catalase) was loaded. dSTORM images were acquired by a commercially available Nikon system based on an inverted microscope (Nikon T*i*-E) equipped with an oil-immersion TIRF objective (Apochromat TIRF100X, 1.49 NA; Nikon) as well as four lasers and a filter set suitable for multiple color imaging. L-function was used for examining the bivariate pair correlation between IgG-BCRs and PI(4,5)P2 in the two-color superresolution imaging experiments (Wiegand and Moloney, 2004; Barr et al., 2016). In detail, L-function is a transformation of K-function. The bivariate K-function $K_{12}(r)$ was defined as the expected number of points of pattern 2 within a given distance r of an arbitrary point of pattern 1, divided by the intensity e_2 of points of pattern 2:

$$_{e2}K_{12}r = E\left[\#\begin{pmatrix}\text{points of pattern 2} \le \text{r from} \\ \text{an arbitrary point of pattern 1}\end{pmatrix}\right]$$

where # means "the number of" and E[ ] is the expectation operator under independence of the two-point patterns, $K_{12}(r) = \pi r^2$, without regard to the individual univariate point patterns. It can be difficult to interpret $K_{12}(r)$ visually. Therefore, a square root transformation of K(r) called L-function was used instead:

$$L_{12}(r) = \left(\sqrt{\frac{K_{12}(r)}{\pi}} - r\right)$$

This transformation (L-function) removes the scale dependence of $K_{12}(r)$ for independent patterns and stabilizes the variance. Values of $L_{12}(r) > 0$ indicate that there were on average more points of pattern 2 within distance r of points of pattern 1 as one would expect under independence, thus indicating attraction between the two patterns up to distance r. The L-function analysis used in this study was computed using MATLAB. dSTORM technology was also used for capturing the superresolution images of monoclonal antibody–stained PI(4,5)P2 in 293T cells expressing human WT IgG-BCRs.

Single-molecule tracking and analysis

Single-molecule tracking was performed following our previously published protocol (Liu et al., 2010a; Xu et al., 2016). B cells were labeled with 1 nM Alexa Fluor 647–conjugated goat Fab anti–mouse IgG1 Fc region antibodies for the best resolution of individual fluorescence spots without the need for further extensive photobleaching. Labeled B cells were washed twice before imaging, and images were taken using TIRFM with a 647-nm laser. A subregion of ∼90 × 90 pixels of the available area of the electron-multiplying charge-coupled device chip was used and recorded at 30 frames per second. Single molecules were analyzed as described in our previous study (Liu et al., 2010a) using MATLAB code based on available positional fitting and tracking algorithms. Mean square displacement and diffusion coefficients for each molecule trajectory were calculated from positional coordinates (Liu et al., 2010a).

Online supplemental material

Fig. S1 shows IgG-BCR expression. Fig. S2 shows that Mut7 tail can lower the mechanical force threshold of IgM-BCR. Fig. S3 shows the enrichment of PI(4,5)P2, PS, PI(3,4,5)P3, PA, and DAG in WT, Mut5–, and Mut6–IgG-BCR. Fig. S4 shows the contribution of rapamycin, Myo-inositol, and PIP5K in PI(4,5)P2 manipulation system. Fig. S5 shows the sequence of cytoplasmic tails used in this article.

Acknowledgments

We thank Dr. Chenqi Xu (Institute of Biochemistry and Cell Biology, Shanghai, China), Dr. Mian Long (Chinese Academy of Sciences, Beijing, China), Dr. Hai Qi (Tsinghua University, Beijing, China), Dr. Yujie Sun (Peking University, Beijing, China), and Dr. Wei Chen (Zhejiang University, Hangzhou, China) for helpful discussions. We thank Dr. Hui Zhang (Tsinghua University, Beijing, China) for her technical support on dSTORM imaging experiments.

This work is supported by funds from National Science Foundation of China (81730043 and 81621002) and the Chinese Ministry of Science and Technology (2014CB542500-03).

The authors declare no competing financial interests.

Author contributions: Conceptualization: Z. Wan and W. Liu; Methodology: Z. Wan and W. Liu; Software: H. Xie; Investigation: Z. Wan and W. Liu; Writing, original draft: Z. Wan and W. Liu; Writing, review and editing: Z. Wan, S. Shaheen, Q. Ji, Y. Xu, J.-S. Zheng, F. Wang, J. Lou, W. Chen, and W. Liu; Funding acquisition: W. Liu; Resources: C. Xu, X. Chen, Z. Li, X. Ji, H. Chen, J. Wang, and Z. Tang; Supervision: W. Liu.

Submitted: 8 November 2017
Revised: 6 March 2018
Accepted: 5 April 2018

References

Bachmann, M.F., U.H. Rohrer, T.M. Kündig, K. Bürki, H. Hengartner, and R.M. Zinkernagel. 1993. The influence of antigen organization on B cell responsiveness. *Science.* 262:1448–1451. https://doi.org/10.1126/science.8248784

Banaszynski, L.A., C.W. Liu, and T.J. Wandless. 2005. Characterization of the FKBP.rapamycin.FRB ternary complex. *J. Am. Chem. Soc.* 127:4715–4721. https://doi.org/10.1021/ja043277y

Barr, V.A., E. Sherman, J. Yi, I. Akpan, A.K. Rouquette-Jazdanian, and L.E. Samelson. 2016. Development of nanoscale structure in LAT-based signaling complexes. *J. Cell Sci.* 129:4548–4562.

Burbage, M., S.J. Keppler, F. Gasparrini, N. Martínez-Martín, M. Gaya, C. Feest, M.C. Domart, C. Brakebusch, L. Collinson, A. Bruckbauer, and F.D. Batista. 2015. Cdc42 is a key regulator of B cell differentiation and is required for antiviral humoral immunity. *J. Exp. Med.* 212:53–72. https://doi.org/10.1084/jem.20141143

Chen, X., W. Pan, Y. Sui, H. Li, X. Shi, X. Guo, H. Qi, C. Xu, and W. Liu. 2015. Acidic phospholipids govern the enhanced activation of IgG-B cell receptor. *Nat. Commun.* 6:8552. https://doi.org/10.1038/ncomms9552

Chowdhury, F., I.T. Li, T.T. Ngo, B.J. Leslie, B.C. Kim, J.E. Sokoloski, E. Weiland, X. Wang, Y.R. Chemla, T.M. Lohman, and T. Ha. 2016. Defining Single Molecular Forces Required for Notch Activation Using Nano Yoyo. *Nano Lett.* 16:3892–3897. https://doi.org/10.1021/acs.nanolett.6b01403

Czech, M.P. 2000. PIP2 and PIP3: complex roles at the cell surface. *Cell.* 100:603–606. https://doi.org/10.1016/S0092-8674(00)80696-0

Davey, A.M., and S.K. Pierce. 2012. Intrinsic differences in the initiation of B cell receptor signaling favor responses of human IgG(+) memory B cells over IgM(+) naive B cells. *J. Immunol.* 188:3332–3341. https://doi.org/10.4049/jimmunol.1102322

Dustin, M.L., and L.C. Kam. 2016. Tapping out a mechanical code for T cell triggering. *J. Cell Biol.* 213:501–503. https://doi.org/10.1083/jcb.201605072

Engels, N., L.M. König, C. Heemann, J. Lutz, T. Tsubata, S. Griep, V. Schrader, and J. Wienands. 2009. Recruitment of the cytoplasmic adaptor Grb2 to surface IgG and IgE provides antigen receptor-intrinsic costimulation to class-switched B cells. *Nat. Immunol.* 10:1018–1025. https://doi.org/10.1038/ni.1764

Falkenburger, B.H., J.B. Jensen, E.J. Dickson, B.C. Suh, and B. Hille. 2010. Phosphoinositides: lipid regulators of membrane proteins. *J. Physiol.* 588:3179–3185. https://doi.org/10.1113/jphysiol.2010.192153

Fleire, S.J., J.P. Goldman, Y.R. Carrasco, M. Weber, D. Bray, and F.D. Batista. 2006. B cell ligand discrimination through a spreading and contraction response. *Science.* 312:738–741. https://doi.org/10.1126/science.1123940

Gibson, D.G., L. Young, R.-Y. Chuang, J.C. Venter, C.A. Hutchison III, and H.O. Smith. 2009. Enzymatic assembly of DNA molecules up to several hundred kilobases. *Nat. Methods.* 6:343–345. https://doi.org/10.1038/nmeth.1318

Halet, G. 2005. Imaging phosphoinositide dynamics using GFP-tagged protein domains. *Biol. Cell.* 97:501–518. https://doi.org/10.1042/BC20040080

Hikida, M., S. Casola, N. Takahashi, T. Kaji, T. Takemori, K. Rajewsky, and T. Kurosaki. 2009. PLC-γ2 is essential for formation and maintenance of memory B cells. *J. Exp. Med.* 206:681–689. https://doi.org/10.1084/jem.20082100

Huang, J., V.I. Zarnitsyna, B. Liu, L.J. Edwards, N. Jiang, B.D. Evavold, and C. Zhu. 2010. The kinetics of two-dimensional TCR and pMHC interactions determine T-cell responsiveness. *Nature.* 464:932–936. https://doi.org/10.1038/nature08944

Huse, M., L.O. Klein, A.T. Girvin, J.M. Faraj, Q.-J. Li, M.S. Kuhns, and M.M. Davis. 2007. Spatial and temporal dynamics of T cell receptor signaling with a photoactivatable agonist. *Immunity.* 27:76–88. https://doi.org/10.1016/j.immuni.2007.05.017

Ishiai, M., M. Kurosaki, R. Pappu, K. Okawa, I. Ronko, C. Fu, M. Shibata, A. Iwamatsu, A.C. Chan, and T. Kurosaki. 1999. BLNK required for coupling Syk to PLC γ 2 and Rac1-JNK in B cells. *Immunity.* 10:117–125. https://doi.org/10.1016/S1074-7613(00)80012-6

Kassas, N., P. Tryoen-Tóth, M. Corrotte, T. Thahouly, M.-F. Bader, N.J. Grant, and N. Vitale. 2012. Genetically encoded probes for phosphatidic acid. *Methods Cell Biol.* 108:445–459. https://doi.org/10.1016/B978-0-12-386487-1.00020-1

Kim, S.T., K. Takeuchi, Z.Y. Sun, M. Touma, C.E. Castro, A. Fahmy, M.J. Lang, G. Wagner, and E.L. Reinherz. 2009. The alphabeta T cell receptor is an anisotropic mechanosensor. *J. Biol. Chem.* 284:31028–31037. https://doi.org/10.1074/jbc.M109.052712

Knight, J.D., and J.J. Falke. 2009. Single-molecule fluorescence studies of a PH domain: new insights into the membrane docking reaction. *Biophys. J.* 96:566–582. https://doi.org/10.1016/j.bpj.2008.10.020

Lakadamyali, M., M.J. Rust, and X. Zhuang. 2004. Endocytosis of influenza viruses. *Microbes Infect.* 6:929–936.

Lee, W.Y., and P. Tolar. 2013. Activation of the B cell receptor leads to increased membrane proximity of the Igα cytoplasmic domain. *PLoS One.* 8:e79148. https://doi.org/10.1371/journal.pone.0079148

Lee, M.S., C.R. Glassman, N.R. Deshpande, H.B. Badgandi, H.L. Parrish, C. Uttamapinant, P.S. Stawski, A.Y. Ting, and M.S. Kuhns. 2015. A Mechanical Switch Couples T Cell Receptor Triggering to the Cytoplasmic Juxtamembrane Regions of CD3ζζ. *Immunity.* 43:227–239. https://doi.org/10.1016/j.immuni.2015.06.018

Lemmon, M.A., K.M. Ferguson, R. O'Brien, P.B. Sigler, and J. Schlessinger. 1995. Specific and high-affinity binding of inositol phosphates to an isolated pleckstrin homology domain. *Proc. Natl. Acad. Sci. USA.* 92:10472–10476. https://doi.org/10.1073/pnas.92.23.10472

Liu, W., and Y.H. Chen. 2005. High epitope density in a single protein molecule significantly enhances antigenicity as well as immunogenicity: a novel strategy for modern vaccine development and a preliminary investigation about B cell discrimination of monomeric proteins. *Eur. J. Immunol.* 35:505–514. https://doi.org/10.1002/eji.200425749

Liu, B., W. Chen, B.D. Evavold, and C. Zhu. 2014. Accumulation of dynamic catch bonds between TCR and agonist peptide-MHC triggers T cell signaling. *Cell.* 157:357–368. https://doi.org/10.1016/j.cell.2014.02.053

Liu, W., Z. Peng, Z. Liu, Y. Lu, J. Ding, and Y.H. Chen. 2004. High epitope density in a single recombinant protein molecule of the extracellular domain of influenza A virus M2 protein significantly enhances protective immunity. *Vaccine.* 23:366–371. https://doi.org/10.1016/j.vaccine.2004.05.028

Liu, W., T. Meckel, P. Tolar, H.W. Sohn, and S.K. Pierce. 2010a. Antigen affinity discrimination is an intrinsic function of the B cell receptor. *J. Exp. Med.* 207:1095–1111. https://doi.org/10.1084/jem.20092123

Liu, W., T. Meckel, P. Tolar, H.W. Sohn, and S.K. Pierce. 2010b. Intrinsic properties of immunoglobulin IgG1 isotype-switched B cell receptors promote microclustering and the initiation of signaling. *Immunity.* 32:778–789. https://doi.org/10.1016/j.immuni.2010.06.006

Liu, W., H. Won Sohn, P. Tolar, T. Meckel, and S.K. Pierce. 2010c. Antigen-induced oligomerization of the B cell receptor is an early target of Fc gamma RIIB inhibition. *J. Immunol.* 184:1977–1989. https://doi.org/10.4049/jimmunol.0902334

Liu, W., E. Chen, X.W. Zhao, Z.P. Wan, Y.R. Gao, A. Davey, E. Huang, L. Zhang, J. Crocetti, G. Sandoval, et al. 2012. The scaffolding protein synapse-associated protein 97 is required for enhanced signaling through isotype-switched IgG memory B cell receptors. *Sci. Signal.* 5:ra54. https://doi.org/10.1126/scisignal.2002820

Liu, W., H. Wang, and C. Xu. 2016a. Antigen Receptor Nanoclusters: Small Units with Big Functions. *Trends Immunol.* 37:680–689. https://doi.org/10.1016/j.it.2016.07.007

Liu, Y., L. Blanchfield, V.P. Ma, R. Andargachew, K. Galior, Z. Liu, B. Evavold, and K. Salaita. 2016b. DNA-based nanoparticle tension sensors reveal that T-cell receptors transmit defined pN forces to their antigens for enhanced fidelity. *Proc. Natl. Acad. Sci. USA.* 113:5610–5615. https://doi.org/10.1073/pnas.1600163113

Logan, M.R., and C.A. Mandato. 2006. Regulation of the actin cytoskeleton by PIP2 in cytokinesis. *Biol. Cell.* 98:377–388. https://doi.org/10.1042/BC20050081

Mattila, P.K., C. Feest, D. Depoil, B. Treanor, B. Montaner, K.L. Otipoby, R. Carter, L.B. Justement, A. Bruckbauer, and F.D. Batista. 2013. The actin and tetraspanin networks organize receptor nanoclusters to regulate B cell receptor-mediated signaling. *Immunity.* 38:461–474. https://doi.org/10.1016/j.immuni.2012.11.019

McHeyzer-Williams, L.J., and M.G. McHeyzer-Williams. 2005. Antigen-specific memory B cell development. *Annu. Rev. Immunol.* 23:487–513. https://doi.org/10.1146/annurev.immunol.23.021704.115732

McLaughlin, S., J. Wang, A. Gambhir, and D. Murray. 2002. PIP(2) and proteins: interactions, organization, and information flow. *Annu. Rev. Biophys. Biomol. Struct.* 31:151–175. https://doi.org/10.1146/annurev.biophys.31.082901.134259

Miki, H., K. Miura, and T. Takenawa. 1996. N-WASP, a novel actin-depolymerizing protein, regulates the cortical cytoskeletal rearrangement in a PIP2-dependent manner downstream of tyrosine kinases. *EMBO J.* 15:5326–5335.

Natkanski, E., W.Y. Lee, B. Mistry, A. Casal, J.E. Molloy, and P. Tolar. 2013. B cells use mechanical energy to discriminate antigen affinities. *Science.* 340:1587–1590. https://doi.org/10.1126/science.1237572

Nowosad, C.R., K.M. Spillane, and P. Tolar. 2016. Germinal center B cells recognize antigen through a specialized immune synapse architecture. *Nat. Immunol.* 17:870–877. https://doi.org/10.1038/ni.3458

Owen, D.M., C. Rentero, J. Rossy, A. Magenau, D. Williamson, M. Rodriguez, and K. Gaus. 2010. PALM imaging and cluster analysis of protein heterogeneity at the cell surface. *J. Biophotonics.* 3:446–454. https://doi.org/10.1002/jbio.200900089

Petersen, E.N., H.-W. Chung, A. Nayebosadri, and S.B. Hansen. 2016. Kinetic disruption of lipid rafts is a mechanosensor for phospholipase D. *Nat. Commun.* 7:13873. https://doi.org/10.1038/ncomms13873

Pierce, S.K., and W. Liu. 2010. The tipping points in the initiation of B cell signalling: how small changes make big differences. *Nat. Rev. Immunol.* 10:767–777. https://doi.org/10.1038/nri2853

Raucher, D., T. Stauffer, W. Chen, K. Shen, S. Guo, J.D. York, M.P. Sheetz, and T. Meyer. 2000. Phosphatidylinositol 4,5-bisphosphate functions as a second messenger that regulates cytoskeleton-plasma membrane adhesion. *Cell.* 100:221–228. https://doi.org/10.1016/S0092-8674(00)81560-3

Schamel, W.W., and M. Reth. 2000. Monomeric and oligomeric complexes of the B cell antigen receptor. *Immunity.* 13:5–14. https://doi.org/10.1016/S1074-7613(00)00003-0

Schnyder, T., A. Castello, C. Feest, N.E. Harwood, T. Oellerich, H. Urlaub, M. Engelke, J. Wienands, A. Bruckbauer, and F.D. Batista. 2011. B cell receptor-mediated antigen gathering requires ubiquitin ligase Cbl and adaptors Grb2 and Dok-3 to recruit dynein to the signaling microcluster. *Immunity.* 34:905–918. https://doi.org/10.1016/j.immuni.2011.06.001

Shaheen, S., Z. Wan, Z. Li, A. Chau, X. Li, S. Zhang, Y. Liu, J. Yi, Y. Zeng, J. Wang, et al. 2017. Substrate stiffness governs the initiation of B cell activation by the concerted signaling of PKCβ and focal adhesion kinase. *eLife.* 6:e23060. https://doi.org/10.7554/eLife.23060

Shi, X., Y. Bi, W. Yang, X. Guo, Y. Jiang, C. Wan, L. Li, Y. Bai, J. Guo, Y. Wang, et al. 2013. Ca2+ regulates T-cell receptor activation by modulating the charge property of lipids. *Nature.* 493:111–115. https://doi.org/10.1038/nature11699

Sohn, H.W., P.D. Krueger, R.S. Davis, and S.K. Pierce. 2011. FcRL4 acts as an adaptive to innate molecular switch dampening BCR signaling and enhancing TLR signaling. *Blood.* 118:6332–6341. https://doi.org/10.1182/blood-2011-05-353102

Spillane, K.M., and P. Tolar. 2017. B cell antigen extraction is regulated by physical properties of antigen-presenting cells. *J. Cell Biol.* 216:217–230. https://doi.org/10.1083/jcb.201607064

Stolz, L.E., W.J. Kuo, J. Longchamps, M.K. Sekhon, and J.D. York. 1998. INP51, a yeast inositol polyphosphate 5-phosphatase required for phosphatidylinositol 4,5-bisphosphate homeostasis and whose absence confers a cold-resistant phenotype. *J. Biol. Chem.* 273:11852–11861. https://doi.org/10.1074/jbc.273.19.11852

Su, X., J.A. Ditlev, E. Hui, W. Xing, S. Banjade, J. Okrut, D.S. King, J. Taunton, M.K. Rosen, and R.D. Vale. 2016. Phase separation of signaling molecules promotes T cell receptor signal transduction. *Science.* 352:595–599. https://doi.org/10.1126/science.aad9964

Suh, B.-C., T. Inoue, T. Meyer, and B. Hille. 2006. Rapid chemically induced changes of PtdIns(4,5)P2 gate KCNQ ion channels. *Science.* 314:1454–1457. https://doi.org/10.1126/science.1131163

Takata, M., Y. Homma, and T. Kurosaki. 1995. Requirement of phospholipase C-gamma 2 activation in surface immunoglobulin M-induced B cell apoptosis. *J. Exp. Med.* 182:907–914. https://doi.org/10.1084/jem.182.4.907

Tang, S., Z. Wan, Y. Gao, J.-S. Zheng, J. Wang, Y.-Y. Si, X. Chen, H. Qi, L. Liu, and W. Liu. 2016. Total chemical synthesis of photoactivatable proteins for light-controlled manipulation of antigen–antibody interactions. *Chem. Sci. (Camb.).* 7:1891–1895. https://doi.org/10.1039/C5SC03404C

Tolar, P. 2017. Cytoskeletal control of B cell responses to antigens. *Nat. Rev. Immunol.* 17:621–634. https://doi.org/10.1038/nri.2017.67

Tolar, P., H.W. Sohn, and S.K. Pierce. 2005. The initiation of antigen-induced B cell antigen receptor signaling viewed in living cells by fluorescence resonance energy transfer. *Nat. Immunol.* 6:1168–1176. https://doi.org/10.1038/ni1262

Tolar, P., J. Hanna, P.D. Krueger, and S.K. Pierce. 2009. The constant region of the membrane immunoglobulin mediates B cell-receptor clustering and signaling in response to membrane antigens. *Immunity.* 30:44–55. https://doi.org/10.1016/j.immuni.2008.11.007

Treanor, B., D. Depoil, A. Gonzalez-Granja, P. Barral, M. Weber, O. Dushek, A. Bruckbauer, and F.D. Batista. 2010. The membrane skeleton controls diffusion dynamics and signaling through the B cell receptor. *Immunity.* 32:187–199. https://doi.org/10.1016/j.immuni.2009.12.005

Treanor, B., D. Depoil, A. Bruckbauer, and F.D. Batista. 2011. Dynamic cortical actin remodeling by ERM proteins controls BCR microcluster organization and integrity. *J. Exp. Med.* 208:1055–1068. https://doi.org/10.1084/jem.20101125

Villalobos, C., R.C. Foehring, J.C. Lee, and R. Andrade. 2011. Essential role for phosphatidylinositol 4,5-bisphosphate in the expression, regulation, and gating of the slow afterhyperpolarization current in the cerebral cortex. *J. Neurosci.* 31:18303–18312. https://doi.org/10.1523/JNEUROSCI.3203-11.2011

Wan, Z., and W. Liu. 2012. The growth of B cell receptor microcluster is a universal response of B cells encountering antigens with different motion features. *Protein Cell.* 3:545–558. https://doi.org/10.1007/s13238-012-2054-1

Wan, Z., S. Zhang, Y. Fan, K. Liu, F. Du, A.M. Davey, H. Zhang, W. Han, C. Xiong, and W. Liu. 2013. B cell activation is regulated by the stiffness properties of the substrate presenting the antigens. *J. Immunol.* 190:4661–4675. https://doi.org/10.4049/jimmunol.1202976

Wan, Z., X. Chen, H. Chen, Q. Ji, Y. Chen, J. Wang, Y. Cao, F. Wang, J. Lou, Z. Tang, and W. Liu. 2015. The activation of IgM- or isotype-switched IgG- and IgE-BCR exhibits distinct mechanical force sensitivity and threshold. *eLife.* 4:e06925. https://doi.org/10.7554/eLife.06925

Wang, X., and T. Ha. 2013. Defining single molecular forces required to activate integrin and notch signaling. *Science.* 340:991–994. https://doi.org/10.1126/science.1231041

Wang, J., S. Tang, Z. Wan, Y. Gao, Y. Cao, J. Yi, Y. Si, H. Zhang, L. Liu, and W. Liu. 2016. Utilization of a photoactivatable antigen system to examine B-cell probing termination and the B-cell receptor sorting mechanisms during B-cell activation. *Proc. Natl. Acad. Sci. USA.* 113:E558–E567. https://doi.org/10.1073/pnas.1517612113

Wang, Y., J. Gao, X. Guo, T. Tong, X. Shi, L. Li, M. Qi, Y. Wang, M. Cai, J. Jiang, et al. 2014. Regulation of EGFR nanocluster formation by ionic protein-lipid interaction. *Cell Res.* 24:959–976. https://doi.org/10.1038/cr.2014.89

Weber, M., B. Treanor, D. Depoil, H. Shinohara, N.E. Harwood, M. Hikida, T. Kurosaki, and F.D. Batista. 2008. Phospholipase C-γ2 and Vav cooperate within signaling microclusters to propagate B cell spreading in response to membrane-bound antigen. *J. Exp. Med.* 205:853–868. https://doi.org/10.1084/jem.20072619

Wiegand, T., and K.A. Moloney. 2004. Rings, circles, and null-models for point pattern analysis in ecology. *Oikos.* 104:209–229. https://doi.org/10.1111/j.0030-1299.2004.12497.x

Xu, C., E. Gagnon, M.E. Call, J.R. Schnell, C.D. Schwieters, C.V. Carman, J.J. Chou, and K.W. Wucherpfennig. 2008. Regulation of T cell receptor activation by dynamic membrane binding of the CD3epsilon cytoplasmic tyrosine-based motif. *Cell.* 135:702–713. https://doi.org/10.1016/j.cell.2008.09.044

Xu, L., A. Auzins, X. Sun, Y. Xu, F. Harnischfeger, Y. Lu, Z. Li, Y.H. Chen, W. Zheng, and W. Liu. 2015. The synaptic recruitment of lipid rafts is dependent on CD19-PI3K module and cytoskeleton remodeling molecules. *J. Leukoc. Biol.* 98:223–234. https://doi.org/10.1189/jlb.2A0614-287RR

Xu, L., M. Xia, J. Guo, X. Sun, H. Li, C. Xu, X. Gu, H. Zhang, J. Yi, Y. Fang, et al. 2016. Impairment on the lateral mobility induced by structural changes underlies the functional deficiency of the lupus-associated polymorphism FcγRIIB-T232. *J. Exp. Med.* 213:2707–2727. https://doi.org/10.1084/jem.20160528

Xu, Y., L. Xu, M. Zhao, C. Xu, Y. Fan, S.K. Pierce, and W. Liu. 2014. No receptor stands alone: IgG B-cell receptor intrinsic and extrinsic mechanisms contribute to antibody memory. *Cell Res.* 24:651–664. https://doi.org/10.1038/cr.2014.65

Yeung, T., G.E. Gilbert, J. Shi, J. Silvius, A. Kapus, and S. Grinstein. 2008. Membrane phosphatidylserine regulates surface charge and protein localization. *Science.* 319:210–213. https://doi.org/10.1126/science.1152066

Zeng, Y., J. Yi, Z. Wan, K. Liu, P. Song, A. Chau, F. Wang, Z. Chang, W. Han, W. Zheng, et al. 2015. Substrate stiffness regulates B-cell activation, proliferation, class switch, and T-cell-independent antibody responses in vivo. *Eur. J. Immunol.* 45:1621–1634. https://doi.org/10.1002/eji.201444777

Zhang, F., Z. Wang, M. Lu, Y. Yonekubo, X. Liang, Y. Zhang, P. Wu, Y. Zhou, S. Grinstein, J.F. Hancock, and G. Du. 2014a. Temporal production of the signaling lipid phosphatidic acid by phospholipase D2 determines the output of extracellular signal-regulated kinase signaling in cancer cells. *Mol. Cell. Biol.* 34:84–95. https://doi.org/10.1128/MCB.00987-13

Zhang, J., K. Leiderman, J.R. Pfeiffer, B.S. Wilson, J.M. Oliver, and S.L. Steinberg. 2006. Characterizing the topography of membrane receptors and signaling molecules from spatial patterns obtained using nanometer-scale electron-dense probes and electron microscopy. *Micron.* 37:14–34. https://doi.org/10.1016/j.micron.2005.03.014

Zhang, Y., C. Ge, C. Zhu, and K. Salaita. 2014b. DNA-based digital tension probes reveal integrin forces during early cell adhesion. *Nat. Commun.* 5:5167. https://doi.org/10.1038/ncomms6167